The Astrophysical Journal, 946:37 (22pp), 2023 March 20 https://doi.org/10.3847/1538-4357/acb156

Protracted Timescales for Nebular Processing of First-formed Solids in the Solar System

Prajkta Mane[1,2], Maitrayee Bose[1], Meenakshi Wadhwa[1], and Céline Defouilloy[3,4]
[1] School of Earth and Space Exploration, Arizona State University, Tempe, AZ 85287, USA; pmane@lpi.usra.edu
[2] Lunar and Planetary Institute, Universities Space Research Association, Houston, TX 77058, USA
[3] WiscSIMS, Department of Geoscience, University of Wisconsin-Madison, Madison, WI 53706, USA
[4] CAMECA, F-92622 Gennevilliers Cedex, France

Received 2020 February 1; revised 2023 January 5; accepted 2023 January 6; published 2023 March 24

Abstract

The calcium–aluminum-rich inclusions (CAIs) from chondritic meteorites are the first solids formed in the solar system. Rim formation around CAIs marks a time period in early solar system history when CAIs existed as free-floating objects and had not yet been incorporated into their chondritic parent bodies. The chronological data on these rims are limited. As seen in the limited number of analyzed inclusions, the rims formed nearly contemporaneously (i.e., <300,000 yr after CAI formation) with the host CAIs. Here we present the relative ages of rims around two type B CAIs from NWA 8323 CV3 (oxidized) carbonaceous chondrite using the ^{26}Al–^{26}Mg chronometer. Our data indicate that these rims formed ∼2–3 Ma after their host CAIs, most likely as a result of thermal processing in the solar nebula at that time. Our results imply that these CAIs remained as free-floating objects in the solar nebula for this duration. The formation of these rims coincides with the time interval during which the majority of chondrules formed, suggesting that some rims may have formed in transient heating events similar to those that produced most chondrules in the solar nebula. The results reported here additionally bolster recent evidence suggesting that chondritic materials accreted to form chondrite parent bodies later than the early-formed planetary embryos, and after the primary heat source, most likely ^{26}Al, had mostly decayed away.

Unified Astronomy Thesaurus concepts: Protoplanetary disks (1300); Planet formation (1241); Cosmochemistry (331); Carbonaceous chondrites (200)

1. Introduction

Radiometric dating studies indicate that calcium–aluminum-rich inclusions (CAIs) are the oldest solids formed in the solar system (Amelin et al. 2010; Connelly et al. 2012). Most mineral phases in relatively pristine CAIs formed at high temperatures (starting at ∼1750 K) in the solar nebula (Grossman 1972; Davis & Richter 2014). These refractory inclusions are usually surrounded by a sequence of rims composed of multi-mineralic layers (Wark & Lovering 1977). Various mechanisms have been proposed to explain the formation of such rims, including condensation and subsequent accretion on the CAI (Yurimoto et al. 2008; Simon et al. 2011, 2016; Bolser et al. 2016), crystallization from a melt of the outer region of the CAI produced by flash-heating mechanisms (Han et al. 2020), formation as evaporation residues (Wark & Boynton 2001), and growth of layers as a result of chemical gradients set up during alteration of the interior of the inclusion in a nebular setting (MacPherson et al. 1981). It is possible that more than one of these processes were involved in the formation of distinct layers in these rims (Davis et al. 1986; Murrell & Burnett 1986; Han et al. 2020). Placing time constraints on the formation of the rims is necessary for understanding the duration and conditions under which these processes may have occurred in the early solar system.

The first report of CAI rims showed a mineralogical sequence composed of an innermost spinel-perovskite-hibonite layer, followed by a melilite-anorthite layer, an Al, Ti-rich pyroxene-diopside layer, and an outermost forsterite layer, and these were termed as Wark–Lovering (WL) rims (Wark & Lovering 1977). Other rim sequences that have since been observed around CAIs include spinel/diopside, spinel/anorthite, or melilite/diopside layers (Wark & Lovering 1977; Wark & Boynton 2001). The formation of these various types of rims marks the end of the growth period of CAIs in the solar nebula prior to their incorporation into chondrite parent bodies (i.e., a time period when these objects were formed, melted and/or evaporated in a nebular setting). One of the limiting factors in establishing a precise chronology of rim sequences around CAIs is their thickness (individual mineral layers in the rims are typically <15–20 μm); sufficiently precise isotope analyses for chronological investigations at this scale is a major analytical challenge. Thus far, high spatial resolution ^{26}Al–^{26}Mg chronometry is the only technique that allows precise dating with sub-Ma precision for such CAI rims.

Laser Ablation Multicollector Inductively Coupled Plasma Mass Spectrometry analyses of ^{26}Al–^{26}Mg systematics in three CAIs from Leoville and Allende CV3 carbonaceous chondrites indicated that the time interval between the formation of the interior and the rim (i.e., Δt) was between ∼130,000 and 290,000 yr (Simon et al. 2005). Similarly, a ^{26}Al–^{26}Mg study of a fluffy type A CAI from the Vigarano CV3 reduced carbonaceous chondrite using Secondary Ion Mass Spectrometry (SIMS), showed that the time interval between the formation of its interior and its rim was 0.18 ± 0.07 Ma (Kawasaki et al. 2017). More recently, another ^{26}Al–^{26}Mg investigation of a type B CAI from the Vigarano CV3 carbonaceous chondrite showed that both the interior and rim phases (hibonite, spinel, and diopside) record an initial ^{26}Al/^{27}Al ratio of $(4.94 \pm 0.12) \times 10^{-5}$, indicating that the interior and rim of this CAI formed near-contemporaneously within $\sim 5 \times 10^4$ yr after the beginning of the solar system (Han et al. 2020). Therefore, previous work suggests that the formation of rims around CAIs was restricted to within the first few hundred thousand years of the beginning of the solar system.

Here we have determined the ^{26}Al–^{26}Mg isotope systematics of phases in the interiors and rims of two CAIs using a CAMECA AMETEX NanoSIMS 50L secondary ion mass spectrometer with a spatial resolution of $\sim$2.5 μm. Preliminary ^{26}Al–^{26}Mg isotopic results for these two CAIs were reported by Mane et al. (2015).

2. Methods

2.1. Electron Microprobe and Secondary Electron Microscope Analysis

The two CAIs Ocotillo and Organ Pipe were selected from a thick section of Northwest Africa (NWA) 8323 CV3 (oxidized) chondritic meteorite. The mineralogy of CAIs was characterized using backscattered electron images and elemental X-ray maps obtained with the JEOL JXA-8530F electron microprobe at Arizona State University (ASU) and the FEI Nova NanoSEM 600 field emission gun scanning electron microscope at the Smithsonian National Museum of Natural History. The major elemental abundances of different mineral phases from both CAIs were determined by wavelength dispersive spectroscopy (WDS) spot analyses using the CAMECA SX 100 electron microprobe at the Lunar and Planetary Laboratory, University of Arizona, operated at 15kV and with beam currents of 20 nA, and equal peak and background counting times of 20 s. Various terrestrial mineral standards were used for calibration of elemental abundances as follows: Mg and Si: olivine (Fo$_{92}$); Na: albite; Ca and Al: anorthite; Fe: fayalite; K: orthoclase; Cr: chromite; Ti: rutile; and Mn: rhodonite. Typical detection limits were 0.05% for oxide abundances. Additionally, we measured terrestrial minerals with known compositions to determine the accuracy of our analyses for all elements. In particular, we measured the USNM 137041 anorthite standard from Great Sitkin Island, Alaska, as unknown to determine the accuracy and precision of Na abundances. This anorthite has a relatively low Na$_2$O content of 0.53 wt% (Jarosewich et al. 1980). Our analyses showed Na$_2$O content of 0.54 ± 0.03 (2sd, $n = 15$) for this anorthite. This demonstrates the precision and accuracy of the Na abundances measured by us in the anorthites in the Ocotillo and Organ Pipe CAIs.

2.2. ^{26}Al–^{26}Mg Analyses

Magnesium isotopic ratios and Al/Mg elemental ratios were measured in the SIMS facility at ASU, using the CAMECA NanoSIMS 50L over two analytical sessions, following analytical protocols described in Mane et al. (2022). A gold-coated polished thick section of NWA 8323, containing the two CAIs was sputtered by a 16 keV primary O$^-$ beam with a primary current of $\sim$20–50 pA. The primary beam was rastered over 5×5 μm areas on the sample. Positive secondary ions were collected from the central 2.5×2.5 μm area by using electronic gating. Positive secondary ions of ^{24}Mg$^+$, ^{25}Mg$^+$, ^{26}Mg$^+$, and ^{27}Al$^+$ were collected simultaneously using electron multipliers (EMs) in isotope ratio mode. Potential isobaric interferences were resolved using a mass resolving power (MRP) of >9000 (where MRP = $(1/4) \times (r/L)$; r is the radius of the magnet and L is the width of the portion of the mass peak between 10% and 90% of the maximum intensity, a measure for the steepness of the peak flanks (Hoppe et al. 2013)). We used the Nuclear Magnetic Resonance tool to regulate magnetic field stability. Variation in the magnetic field within an analytical session was <10 ppm.

The Mg isotopic ratios (^{25}Mg/^{24}Mg and ^{26}Mg/^{24}Mg) were corrected for dead time. The instrumental mass bias was corrected using the following natural and synthetic terrestrial standards: San Carlos olivine, San Carlos augite, Lake County plagioclase, and synthetic NIST SRM 610 glass. Analysis time varied between 10 and 90 minutes per spot for different mineral phases to optimize the total counts of the secondary ions. Each spot was pre-sputtered with a higher current ($\sim$100 pA) until the secondary counts were stabilized ($\sim$3–5 minutes) before each analysis.

The instrumental mass fractionation (IMF) is defined as

$$\alpha_{25,26} = \frac{(^{25,26}\mathrm{Mg}/^{24}\mathrm{Mg})_m}{(^{25,26}\mathrm{Mg}/^{24}\mathrm{Mg})_{\mathrm{true}}},$$

where m denotes the measured ratio and true ratios are the Mg isotopic ratios $(^{25}\mathrm{Mg}/^{24}\mathrm{Mg})_{\mathrm{ref}} = 0.12663$ and $(^{26}\mathrm{Mg}/^{24}\mathrm{Mg})_{\mathrm{ref}} = 0.13932$ (Catanzaro et al. 1966). The IMF follows the following exponential mass fractionation relationship:

$$\alpha_{25} = (\alpha_{26})^{\beta}.$$

The quantity β is the IMF factor of 0.5128 (Davis et al. 2015)

$$\delta^{25,26}\mathrm{Mg}' = \ln\alpha_{25,26} \times 1000.$$

The radiogenic excess in ^{26}Mg is then calculated as

$$\Delta^{26}\mathrm{Mg}^* = \delta^{26}\mathrm{Mg} - [(1 + \delta^{25}\mathrm{Mg}/1000)^{1/\beta} - 1] \times 1000.$$

The δ^{26}Mg* and external reproducibilities (2σ) based on repeat analyses of terrestrial standards with different Al/Mg ratios are as follows: San Carlos olivine δ^{26}Mg* = -1.4 ± 3.2‰; San Carlos augite δ^{26}Mg* = 0.8 ± 2.6‰; NIST SRM 610 δ^{26}Mg* = 5.6 ± 7.1‰; and Lake County plagioclase δ^{26}Mg* = -3.2 ± 11.9‰ (Figures 13–16).

The ^{27}Al/^{24}Mg (atomic) ratios of the unknown samples were determined using the following natural and synthetic terrestrial standards: San Carlos olivine (^{27}Al/^{24}Mg = 0.0006), San Carlos augite (^{27}Al/^{24}Mg = 0.65), NIST SRM 610 (^{27}Al/^{24}Mg = 28.4), and Lake County plagioclase (^{27}Al/^{24}Mg = 255). The relative sensitivity factor (RSF) for each standard was calculated by comparing the true ^{27}Al/^{24}Mg ratio with the ^{27}Al/^{24}Mg ratios measured using NanoSIMS:

$$\mathrm{RSF} = (^{27}\mathrm{Al}/^{24}\mathrm{Mg})_{\mathrm{true}}/(^{27}\mathrm{Al}/^{24}\mathrm{Mg})_{\mathrm{measured}}.$$

This RSF value was then used to calculate the true ^{27}Al/^{24}Mg ratio of unknown samples:

$$(^{27}\mathrm{Al}/^{24}\mathrm{Mg})_{\mathrm{true}} = \mathrm{RSF} \times (^{27}\mathrm{Al}/^{24}\mathrm{Mg})_{\mathrm{measured}}.$$

The uncertainties for the Mg isotopic compositions (2σ) reported in Tables 1 and 2 are calculated as

$$\sigma_{\mathrm{final}} = \sqrt{\sigma^2_{\mathrm{internal}} + \sigma^2_{\mathrm{external}}},$$

where $\sigma_{\mathrm{internal}}$ is the standard error of the mean of the Δ^{26}Mg* of each unknown and $\sigma_{\mathrm{external}}$ is the standard error of the mean of repeated measurements of the terrestrial standards. The uncertainties for Al/Mg ratios are calculated based on the percentage reproducibility (2σ) of repeated analyses of the terrestrial standards with the most similar Al/Mg ratios.

Table 1

^{26}Al–^{26}Mg Systematics in Minerals in the Interior and Rim of the Ocotillo CAI

	δ^{25}Mg	2σ	Δ^{26}Mg*	2σ	^{27}Al/^{24}Mg	2σ
Interior						
Interior anorthite-i	10.7	4.3	88.0	20.3	286.1	37.1
Interior anorthite-ii	1.5	4.7	183.6	22.5	485.4	37.1
Interior anorthite-iii	5.9	3.5	81.9	16.8	207.6	37.1
Interior anorthite-iv	6.5	3.9	115.6	18.8	293.1	37.1
Interior anorthite-v	3.2	4.7	185.9	22.5	451.0	37.1
Interior anorthite-vi	2.9	4.6	163.3	21.9	430.8	37.1
Interior anorthite-vii	−1.7	4.9	200.5	23.2	489.3	37.1
Interior anorthite-viii	5.5	2.5	22.3	12.9	55.4	37.1
Interior anorthite-ix	−4.3	4.2	92.1	19.5	341.7	37.1
Interior anorthite-x	3.7	2.9	35.2	14.3	92.8	37.1
Interior anorthite-xi	−0.8	3.3	122.9	16.3	259.6	37.1
Interior anorthite-xii	1.3	3.3	20.1	15.9	87.0	37.1
Interior pyroxene-i	−2.3	2.5	4.3	8.2	5.9	2.3
Interior pyroxene-ii	−0.9	2.4	4.9	7.8	5.7	2.3
Interior pyroxene-iii	0.8	2.4	5.1	7.9	6.0	2.3
Interior spinel-i	−2.5	2.6	6.1	8.8	4.4	2.3
Interior spinel-ii	1.1	2.4	6.6	7.8	3.5	2.3
Interior spinel-iii	0.2	2.4	6.4	7.8	4.5	2.3
Rim						
Rim anorthite-i	3.0	2.6	2.2	13.2	43.2	2.3
Rim anorthite-ii	−5.8	4.0	9.4	18.5	151.1	37.1
Rim anorthite-iii	−3.7	2.8	4.8	6.9	31.2	2.3
Rim anorthite-iv	−4.9	3.3	5.5	15.7	144.5	37.1
Rim anorthite-v	1.5	3.3	5.8	12.2	30.1	2.3
Rim anorthite-vi	1.7	3.3	8.5	16.0	79.2	37.1
Rim anorthite-vii	2.4	3.0	4.0	14.6	109.9	37.1
Rim anorthite-viii	−13.6	4.5	23.2	20.5	423.1	37.1
Rim anorthite-ix	8.5	4.0	10.8	18.4	69.1	37.1
Rim anorthite-x	10.5	2.6	4.5	13.3	39.7	2.3
Rim anorthite-xi	2.3	2.9	8.0	14.5	246.5	37.1
Rim anorthite-xii	−3.2	3.7	21.7	17.2	274.7	37.1
Rim spinel-i	−0.7	1.0	2.3	2.9	1.8	0.3
Rim spinel-ii	3.9	2.7	4.5	3.7	2.5	0.3
Rim pyroxene-i	1.0	2.7	4.6	4.2	7.9	2.3

Table 2

^{26}Al–^{26}Mg Systematics in Minerals in the Interior and Rim of the Organ Pipe CAI

	δ^{25}Mg	2σ	Δ^{26}Mg*	2σ	^{27}Al/^{24}Mg	2σ
Interior						
Interior anorthite-i	2.5	4.4	131.4	16.1	385.0	37.1
Interior anorthite-ii	−3.5	4.2	100.9	15.6	281.5	37.1
Interior anorthite-iii	−12.2	6.1	298.7	20.6	712.8	37.1
Interior anorthite-iv	−5.7	6.3	328.7	21.1	792.5	37.1
Interior anorthite-v	−4.7	5.6	241.9	19.2	644.0	37.1
Interior anorthite-vi	−3.0	4.4	123.1	16.1	277.4	37.1
Interior anorthite-vii	−1.4	4.6	159.3	16.4	459.1	37.1
Interior anorthite-viii	12.6	4.0	153.0	15.2	420.7	37.1
Interior anorthite-ix	−27.2	5.4	331.0	16.1	811.5	37.1
Interior spinel-i	2.3	2.4	10.1	7.5	2.4	0.3
Interior spinel-ii	3.0	2.4	12.0	7.5	2.1	0.3
Interior spinel-iii	−0.3	2.4	2.5	7.6	2.4	0.3
Interior pyroxene-i	0.6	2.5	13.6	7.8	11.4	2.3
Interior pyroxene-ii	0.6	2.6	16.7	7.9	8.3	2.3
Interior pyroxene-iii	−1.8	2.9	7.2	8.7	17.0	2.3
Interior pyroxene-iv	0.5	2.7	6.4	8.1	8.3	2.3
Interior pyroxene-v	−1.9	2.7	4.3	8.3	11.1	2.3
Rim						
Rim anorthite-i	−3.6	2.5	5.3	12.8	112.0	37.1
Rim anorthite-ii	−2.6	2.7	6.5	9.0	37.8	2.3
Rim anorthite-iii	−0.1	2.6	12.2	13.3	199.7	37.1
Rim anorthite-iv	5.7	2.6	−2.8	13.2	129.6	37.1
Rim anorthite-v	−3.6	2.5	6.2	12.7	92.7	37.1
Rim anorthite-vi	3.2	2.4	17.5	12.6	75.4	37.1
Rim anorthite-vii	−3.0	2.5	18.7	12.9	348.3	37.1
Rim anorthite-viii	−3.1	2.4	8.4	12.5	101.9	37.1
Rim anorthite-xi	−10.1	3.1	16.5	15.0	320.8	37.4
Rim anorthite-x	−1.5	2.7	4.7	13.5	203.5	37.4
Rim spinel-i	−0.4	1.0	1.8	2.8	2.2	0.3
Rim pyroxene-i	3.6	2.4	10.7	7.6	11.9	2.3
Rim pyroxene-ii	−0.2	2.2	3.4	11.9	3.9	0.3
Rim pyroxene-iii	1.6	2.4	3.0	2.6	7.7	2.3

2.3. *Oxygen Isotopic Analyses*

The oxygen three-isotopic analysis was performed using the CAMECA IMS-1280 ion microprobe at WiscSIMS lab, University of Wisconsin, Madison, using analytical protocols similar to those of Kita et al. (2010) and Ushikubo et al. (2017). A Cs^+ beam with ∼20 pA primary current was used to sputter a ∼3 μm spot to target smaller phases in the rims and CAI interiors. The normal incidence electron gun was used for charge compensation. Each spot was pre-sputtered for 120 s before the analysis. Secondary ion species of $^{16}O^-$ (Faraday cup), $^{17}O^-$ and $^{18}O^-$ (EMs) were simultaneously detected with typical $^{17}O^-$ count rates of ∼(6–8) × 10^3 cps and with a mass resolving power of ∼6000. The contribution of the tailing of $^{16}OH^-$ interference on $^{17}O^-$ was corrected using the method described by Heck et al. (2010), and was always lower than 0.3‰. San Carlos olivine (SC-Ol) was used as a bracketing standard ($\delta^{18}O = 5.32$‰; Kita et al. 2010) to correct for instrumental mass bias (each series of 10–15 sample analyses bracketed with 8 SC-Ol analyses). Terrestrial spinel, gehlenitic and åakermanitic melilites, anorthite, diopside, and synthetic fassaite glasses were used to correct for matrix effects. The measured $^{17}O/^{16}O$ and $^{18}O/^{16}O$ ratios were reported relative to VSMOW (Vienna Standard Mean Ocean Water). The relative deviation from the reference isotopic composition is expressed as $\delta^{17,18}O$, where

$$\delta^{17,18}O = [(^{17,18}O/^{16}O)_{\rm measured}/(^{17,18}O/^{16}O)_{\rm ref} - 1] \times 1000({\rm permil}).$$

The $\Delta^{17}O$ value was calculated as follows:

$$\Delta^{17}O = \delta^{17}O - \delta^{18}O \times 0.52$$

The external reproducibilities (2σ) reported in Tables 3 and 4 are based on eight bracketed analyses of the SC-Ol standard (typically ∼±1–2‰ for $\delta^{17}O$, $\delta^{18}O$, and $\Delta^{17}O$) and were taken to represent the analytical uncertainties on individual SIMS analyses; these were similar to internal errors based on counting statistics on individual analyses. After the analyses, SIMS pits were verified using the electron microprobe at ASU to make sure there was no overlap with cracks, inclusions, or other phases.

2.4. *Trace Elements Analyses*

The abundances of Ba, Sr, and Eu in the anorthites in the rims and interiors of the two CAIs were analyzed using a CAMECA IMS-6f SIMS at ASU using the protocols described in Zinner & Crozaz (1986) and Hinton (1990). A O^- primary beam with a current of ∼15 nA was used to sputter an area of ∼20 × 20 μm^2. A combination of a 400 μm contrast aperture

Table 3
Oxygen Isotopic Compositions of Minerals in the Interior and Rim of the Ocotillo CAI

	$\delta^{17}O$	2σ	$\delta^{18}O$	2σ	$\Delta^{17}O$	2σ
Interior anorthite-a	8.10	0.80	1.50	1.93	−2.72	1.96
Interior anorthite-b	8.30	0.80	2.96	1.93	−1.35	1.96
Interior anorthite-c	4.94	0.80	0.10	1.93	−2.47	1.96
Interior anorthite-d	−10.14	0.80	−14.36	1.93	−9.09	1.96
Interior anorthite-e	−13.74	0.80	−18.60	1.93	−11.46	1.96
Interior anorthite-f	8.96	0.80	2.96	1.93	−1.70	1.96
Interior spinel-a	−45.17	1.16	−47.36	2.44	−23.87	2.27
Interior spinel-b	−44.48	1.16	−48.55	2.44	−25.42	2.27
Interior pyroxene-a	−35.30	0.85	−39.10	1.09	−20.75	1.24
Interior pyroxene-b	−33.21	0.85	−37.29	1.09	−20.02	1.24
Interior pyroxene-c	−40.32	1.16	−42.05	2.44	−21.09	2.27
Interior pyroxene-d	−42.52	1.16	−46.24	2.44	−24.13	2.27
Interior melilite-a	4.69	1.16	−1.16	2.44	−3.59	2.27
Interior melilite-b	2.71	1.16	−2.87	2.44	−4.28	2.27
Interior melilite-c	2.77	1.16	−1.84	2.44	−3.28	2.27
Interior melilite-d	4.15	0.85	0.20	1.09	−1.96	1.24
Interior melilite-f	7.16	0.85	1.53	1.09	−2.19	1.24
Rim anorthite-a	8.67	0.80	1.67	1.93	−2.84	1.96
Rim anorthite-b	8.38	0.80	4.11	1.93	−0.25	1.96
Rim anorthite-c	9.87	0.80	2.34	1.93	−2.79	1.96
Rim spinel-a	−38.15	1.16	−38.58	2.44	−18.74	2.27
Rim spinel-b	−38.27	1.16	−42.21	2.44	−22.30	2.27
Rim spinel-c	−40.85	0.85	−43.60	1.09	−22.36	1.24
Rim pyroxene-a	−18.19	1.16	−22.40	2.44	−12.94	2.27
Rim pyroxene-b	−18.47	1.16	−22.82	2.44	−13.22	2.27
Rim pyroxene-c	−15.33	0.85	−19.52	1.09	−11.55	1.24
Rim pyroxene-d	−41.64	1.16	−45.44	2.44	−23.79	2.27

Table 4
Oxygen Isotopic Compositions of Minerals in the Interior and Rim of the Organ Pipe CAI

	$\delta^{17}O$	2σ	$\delta^{18}O$	2σ	$\Delta^{17}O$	2σ
Interior anorthite-a	−8.23	0.74	−13.53	1.71	−9.25	1.86
Interior anorthite-b	−5.43	0.74	−11.68	1.71	−8.86	1.86
Interior anorthite-c	−2.42	0.74	−6.43	1.71	−5.17	1.86
Interior anorthite-d	−5.41	0.97	−11.15	1.39	−8.33	1.60
Interior anorthite-e	9.83	0.97	3.35	1.39	−1.76	1.60
Interior anorthite-f	9.74	0.74	3.32	1.71	−1.74	1.86
Interior spinel-a	−43.90	0.97	−46.97	1.39	−24.15	1.60
Interior spinel-b	−43.46	0.97	−46.85	1.39	−24.25	1.60
Interior pyroxene-a	−37.76	0.97	−41.40	1.39	−21.77	1.60
Interior pyroxene-b	−43.66	0.97	−46.91	1.39	−24.20	1.60
Interior melilite-a	7.15	0.97	2.89	1.39	−0.83	1.60
Interior melilite-b	−2.34	0.74	−6.72	1.71	−5.50	1.86
Interior melilite-c	−9.75	0.97	−14.25	1.39	−9.19	1.60
Rim anorthite-a	8.73	0.74	2.33	1.71	−2.21	1.86
Rim anorthite-b	5.47	0.74	−0.83	1.71	−3.67	1.86
Rim anorthite-c	7.49	0.74	2.97	1.71	−0.92	1.86
Rim anorthite-d	9.75	0.74	2.38	1.71	−2.69	1.86
Rim spinel-a	−44.43	0.74	−47.23	1.71	−24.13	1.86
Rim spinel-b	−42.04	0.74	−44.35	1.71	−22.49	1.86
Rim spinel-c	−45.00	0.97	−48.22	1.39	−24.82	1.60
Rim spinel-d	−43.86	0.97	−46.92	1.39	−24.12	1.60
Rim pyroxene-a	−44.58	0.97	−46.35	1.39	−23.17	1.60
Rim pyroxene-b	−7.27	0.74	−11.83	1.71	−8.04	1.86
Rim pyroxene-c	−34.81	0.97	−40.45	1.39	−22.35	1.60

and a 100 μm field aperture was used to target the analysis area of ∼4 μm diameter. $^{28}Si^+$, $^{88}Sr^+$, $^{138}Ba^+$, and $^{151}Eu^+$ secondary species were detected on an EM in a pulse counting mode, with an MRP of ∼900. Five cycles of mass calibration were performed before every analysis to minimize the possible hysteresis effects of the magnetic field control. Energy filtering was used to minimize molecular interferences, with an energy offset of ∼75 eV and energy slit width of 40 eV. A presputtering time of 300 s was applied before every analysis. To calculate elemental abundances in ppm, calibration was done using synthetic standard glasses, NIST 610, NIST 612, and NIST 614, and basaltic standards ML3BG and KL2G. Each analysis lasted for ∼1.5 hr with 30 cycles. The $^{151}Eu^+$ signal has a molecular interference from $^{135}Ba^{16}O^+$ species that was corrected empirically with $BaO^+/Ba^+ = 0.049$ as reported for silicates (Hinton 1990; Dunham et al. 2019) and using methods described in Zinner & Crozaz (1986).

The RSF is calculated as

$$RSF = (C_x/C_{Si}) \times (I_{Si}/I_x),$$

where C_x is the known concentration of the element of interest, C_{Si} is the known concentration of Si, I_x is the secondary ion intensity of the element of interest, and I_{Si} is the secondary ion intensity of Si. The RSF values for Sr, Ba, and Eu in our analytical session were 0.11, 0.04, and 0.12, respectively. The uncertainties on Ba/Sr and Eu/Sr ratios in anorthite in the interiors and rims of Ocotillo and Organ Pipe (reported in Table 5) are based on the counting statistics. Although the rim analysis spots were targeted on anorthites, because of their fine grain size, there may have been an overlap on other phases.

3. Results

3.1. Sample Mineralogy and Composition

The NWA 8323 chondrite displays a black to dark gray interior and consists of abundant chondrules, CAIs, and amoeboid olivine aggregates set in a fine-grained, almost opaque matrix. Chondrules are typically 0.5–1 mm in size whereas Fe–Ni metal is rare. This meteorite has a low weathering grade and shock stage (Ruzicka et al. 2015).

One of the CAIs, designated Ocotillo, is a coarse-grained type B inclusion (∼6 × 4 mm) consisting of melilite, spinel, anorthite, and Al, Ti-rich pyroxene (Figures 8–9). It has a rim sequence consisting of anorthite, spinel, and pyroxene. As viewed in the thick section, it is irregularly donut-shaped with an undulating surface with embayments filled with carbonaceous chondrite matrix (Figure 8). The CAI shows little secondary alteration, with the rare occurrence of nepheline. Melilite occurs as irregular to blocky grains with spinel inclusions inside them (Figures 1(a)–(c)). The WDS elemental data of the Ocotillo mineral phases are reported in Appendix A (Table 6). The MgO content of melilite in the interior of Ocotillo varies from 2.2–6.3 wt% ($Åk_{15}$ to $Åk_{43}$). Pyroxene in the interior of this CAI is anhedral and contains 19–25 wt% Al_2O_3 and 0–15 wt% TiO_2. Anorthite in the interior also occurs as irregular to subhedral grains with nearly end-member $CaAl_2Si_2O_8$ composition (>An_{99}). Spinel in the interior occurs as euhedral grains, often in clusters. Compositionally spinel is close to end-member $MgAl_2O_4$ with a trace amount of Ti (0.2–0.7 wt% TiO_2) and Cr (0.1–0.3 wt% Cr_2O_3). The rim sequence around Ocotillo has an innermost anorthite layer, intermediate spinel layer, and outermost pyroxene layer. The innermost anorthite layer contains irregular to blocky anorthite (Figures 1(a)–(c)). The rim anorthite is compositionally nearly end-member $CaAl_2Si_2O_8$ (>An_{99}). The anorthite layer is

Table 5
Ba/Sr and Eu/Sr Ratios in the Interior and Rim Anorthites of Ocotillo and Organ Pipe CAIs

	Ba/Sr	2σ	Eu/Sr	2σ
Ocotillo interior-1	0.44	0.02	0.74	0.19
Ocotillo interior-2	0.84	0.06	1.96	0.58
Ocotillo interior-3	0.48	0.04	0.72	0.29
Ocotillo rim-1	0.69	0.05	1.73	0.49
Ocotillo rim-2	1.69	0.08	0.64	0.23
Ocotillo rim-3	1.33	0.05	0.68	0.20
Ocotillo rim-4	1.07	0.04	0.59	0.18
Organ Pipe interior-1	0.30	0.02	0.77	0.22
Organ Pipe interior-2	0.15	0.02	0.86	0.28
Organ Pipe interior-3	0.55	0.08	1.31	0.77
Organ Pipe rim-1	0.55	0.04	0.42	0.21
Organ Pipe rim-2	1.17	0.07	0.07	0.06
Organ Pipe rim-3	0.78	0.11	2.04	1.13
Organ Pipe rim-4	2.16	0.17	1.83	0.87
Organ Pipe rim-5	1.71	0.10	0.94	0.38
Organ Pipe rim-6	1.38	0.07	0.39	0.19
Organ Pipe rim-7	0.51	0.05	0.29	0.22
Organ Pipe rim-8	0.28	0.04	0.59	0.39
Organ Pipe rim-9	0.28	0.04	0.59	0.39

irregular in its thickness and shows a sharp boundary with interior melilite. The grain size of anorthite in this layer is ∼10–15 μm (Figure 1(b)). The anorthite grains in this layer show equant to lath-like habit (Figures 1(a)–(c)). The intermediate spinel layer shows euhedral to anhedral grains. Spinel contains minor FeO (1.4–4.5 wt%) and a trace amount of Ti (0.2–0.5 wt% TiO_2) and Cr (0.2–0.3 wt% Cr_2O_3). In some places, there is a presence of an unidentified, possibly glassy layer of non-stoichiometric composition between anorthite and spinel (Figure 1(c)). The outermost pyroxene layer is finer grained compared to the anorthite and spinel layers. The rim pyroxene contains 12–18 wt% MgO, 1.5–17 wt% Al_2O_3, 0.4–12.8 wt% FeO, and 0–5 wt% TiO_2. There are two occurrences of residual perovskite grains near the boundary of interior melilite and rim anorthite.

The second CAI, designated Organ Pipe, is also a coarse-grained type B inclusion (∼1.5×3 mm) with mineralogy similar to Ocotillo (Figures 10–11). As viewed in the thick section, it is boomerang-shaped, with well-developed rims on the convex side whereas there are only partially developed rims on the concave side (Figure 10). Melilite in the interior of Organ Pipe occurs as irregular to blocky grains with spinel inclusions inside them (Figures 1(d)–(f)). The WDS elemental data of mineral phases in Organ Pipe is reported in Appendix A (Table 7). The MgO content of melilite in the interior of this CAI varies from 1.5–4.7 wt% (Åk_{10} to Åk_{32}). Pyroxene in the interior is anhedral and contains 16–22 wt% Al_2O_3 and 6–11 wt% TiO_2. Anorthite in the interior also occurs as irregular to subhedral grains with nearly end-member $CaAl_2Si_2O_8$ composition (>An_{99}). Spinel in the interior occurs as euhedral grains, often in clusters. Compositionally, spinel is nearly end-member $MgAl_2O_4$ with a trace amount of Ti (0.2–0.4 wt% TiO_2) and Cr (0.1–0.2 wt% Cr_2O_3). Organ Pipe also contains refractory metal nuggets. The convex side of Organ Pipe shows a well-developed rim sequence with the innermost anorthite layer, intermediate spinel layer, and outermost pyroxene layer (Figure 1(d)). The rim anorthite is compositionally nearly end-member $CaAl_2Si_2O_8$ (>An_{99}). Similar to the rim anorthite in Ocotillo, the rim anorthite in Organ Pipe also shows irregular thickness, a sharp boundary with interior melilite, and occasional veins and embayments into the interior melilite (Figure 1(d), (f)). The grain size of the rim anorthite is ∼10–15 μm (Figures 1(f) and 12). The intermediate spinel layer shows euhedral to anhedral spinel with minor FeO (0.5–5.9 wt%) and trace amounts of Ti (0.2–0.7 wt% TiO_2) and Cr (0.1–0.2 wt% Cr_2O_3). The outermost pyroxene layer is finer grained compared to the grain sizes in the anorthite and spinel layers. The pyroxene contains 13–24 wt% MgO, 4–12 wt% Al_2O_3, and 0.7–10.6 wt% FeO. On the concave side of the inclusion, there is a fine-grained (grain size ∼ 1–2 μm) spinel layer in contact with blocky interior anorthite (Figure 1(d)).

3.2. ^{26}Al–^{26}Mg Chronology

The ^{26}Al–^{26}Mg data for individual phases in the interiors and the rims of the Ocotillo and Organ Pipe CAIs are given in Tables 1 and 2, and are illustrated in Figure 2. The phases in the interior of Ocotillo define an isochron that corresponds to a $^{26}\text{Al}/^{27}\text{Al}$ ratio of $(5.2 \pm 0.2) \times 10^{-5}$, while phases in the rim around Ocotillo define a distinct isochron with a shallower slope corresponding to a $^{26}\text{Al}/^{27}\text{Al}$ ratio of $(5.8 \pm 2.1) \times 10^{-6}$ (Figure 2(a)). The interior and rim isochrons of both CAIs show positive $(\delta^{26}\text{Mg}^*)_0$ values outside the analytical error, suggesting multiple episodes of heating and recrystallization. The difference in the slopes of these two isochrons corresponds to a time interval of $2.3^{+0.5}_{-0.4}$ Ma. Similarly, the phases in the interior of Organ Pipe define an isochron corresponding to a $^{26}\text{Al}/^{27}\text{Al}$ ratio of $(5.3 \pm 0.1) \times 10^{-5}$, while the phases in the rim of Organ Pipe yield a distinct isochron with $^{26}\text{Al}/^{27}\text{Al}$ ratio of $(5.5 \pm 1.8) \times 10^{-6}$ (Figure 2(b)). The difference in the slopes of these two isochrons corresponds to a time interval of $2.4^{+0.9}_{-0.5}$ Ma.

3.3. Oxygen Isotopic Composition

Oxygen isotopic compositions of minerals in Ocotillo and Organ Pipe are given in Tables 3 and 4, and show significant variation in the interiors as well as rims (Figure 3(a), (b)). In terms of Δ^{17}O, phases in the two CAIs range from ^{16}O-rich composition ($\Delta^{17}\text{O} \sim -25‰$) to up to the terrestrial value ($\Delta^{17}\text{O} \sim 0‰$). The interior spinels in both CAIs show a uniform Δ^{17}O value of $-24 \pm 2‰$ (2SD). The interior pyroxenes also show a restricted range in Δ^{17}O of $-24.2 \pm 1.6‰$ to $-20 \pm 1‰$. The interior melilites show Δ^{17}O values that are close to terrestrial composition (ranging from $-9 \pm 2‰$ to $-1 \pm 2‰$). The interior anorthites show a range in Δ^{17}O of $-11 \pm 2‰$ to $-1 \pm 2‰$. The rim spinels in both CAIs show a restricted range in Δ^{17}O of $-19 \pm 2‰$ to $-22 \pm 2‰$. The rim pyroxenes show Δ^{17}O values ranging from $-24 \pm 2‰$ to $-8 \pm 2‰$. The rim anorthites show Δ^{17}O values in the range of $-4 \pm 2‰$ to $0 \pm 2‰$.

3.4. Trace Elemental Composition

The Ba/Sr and Eu/Sr ratios in anorthites in the interiors and the rims of Ocotillo and Organ Pipe are reported in Table 5. Anorthites in the interior of Ocotillo show Ba/Sr ratios ranging from 0.4–0.8, whereas the rim anorthites in this CAI show a range of 0.7–1.7. Anorthites in the interior of Ocotillo show Eu/Sr ratios ranging from 0.7–2.0, whereas the rim anorthites of Ocotillo show a range of 0.6–1.7. Anorthites in the interior of Organ Pipe show Ba/Sr ratios ranging from 0.1–0.5, whereas the rim anorthites show a range of 0.3–2.2 in this CAI. Anorthites in the interior of Organ Pipe show Eu/Sr ratios ranging from 0.8–1.3, whereas the rim anorthites in this CAI show a range of 0.1–2.0.

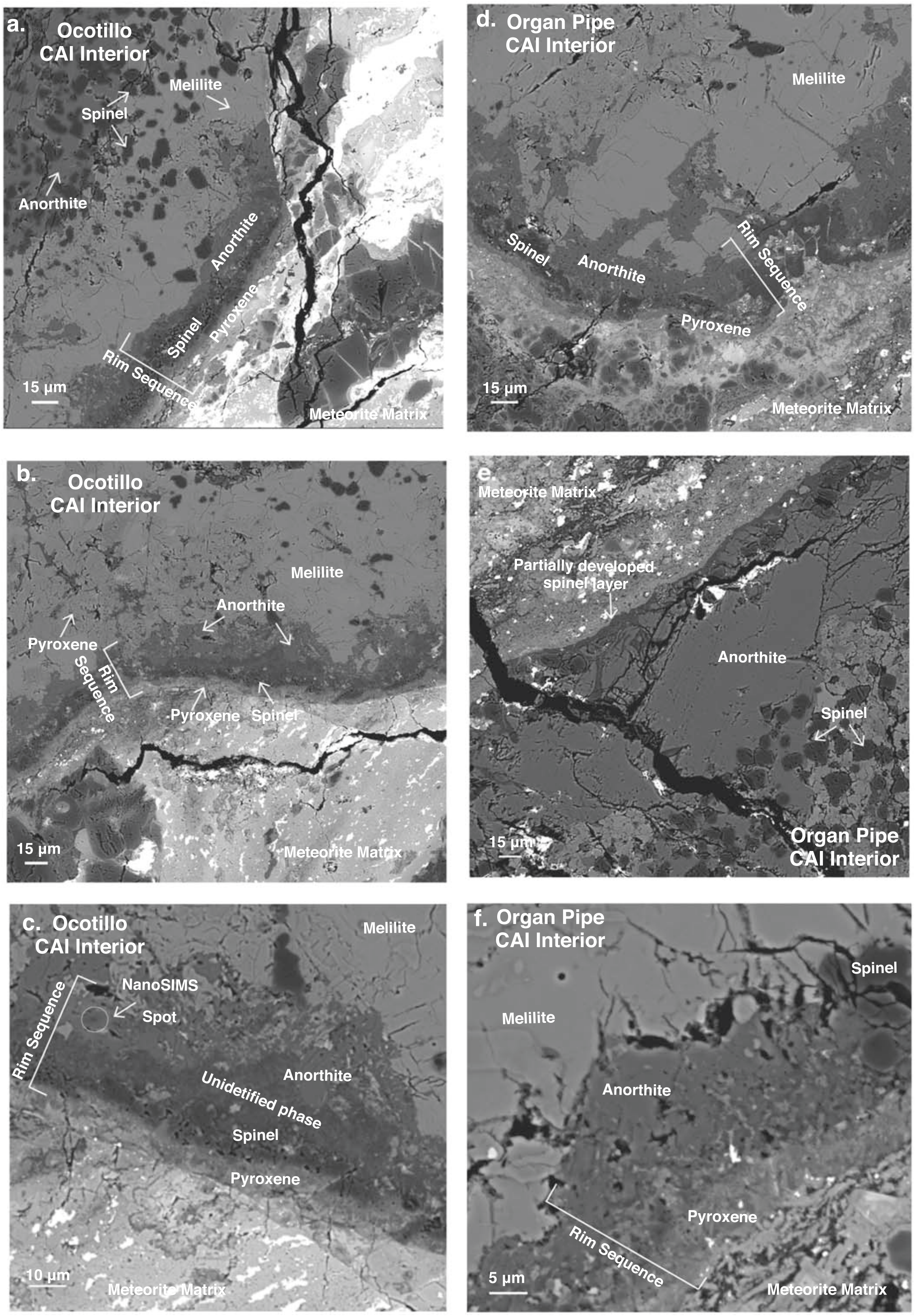

Figure 1. High-resolution backscattered electron images of various regions in the CAIs Ocotillo and Organ Pipe.

4. Discussion

4.1. Geochemical and Oxygen Isotopic Characteristics of Ocotillo and Organ Pipe

In CAIs, anorthite can form as a condensate, or as a product of crystallization from a melt. Additionally, it can form as an alteration product either in a nebular or a parent body setting (MacPherson 2014). Some CAIs from the Allende CV3 carbonaceous chondrite show an outer alteration domain (close to the WL rims) that contains secondary anorthite, feldspathoids, FeO-bearing spinel, and grossular, and records an alteration event for these CAIs at ~2–3 Ma after the primary CAI formation event (Fagan et al. 2007). The timing of this alteration event is consistent with nebular timescales, but an alteration in parent body settings cannot be ruled out. A pyroxene-anorthite-rich CAI from the Acfer 094 C-ungrouped 3.00 chondrite records a canonical $^{26}\mathrm{Al}/^{27}\mathrm{Al}$ ratio in its melilite and diopside, but has a lower $^{26}\mathrm{Al}/^{27}\mathrm{Al}$ ratio of $(5.21 \pm 0.54) \times 10^{-6}$ recorded in its anorthite. This anorthite also shows a ^{16}O-rich composition, suggesting that it formed as

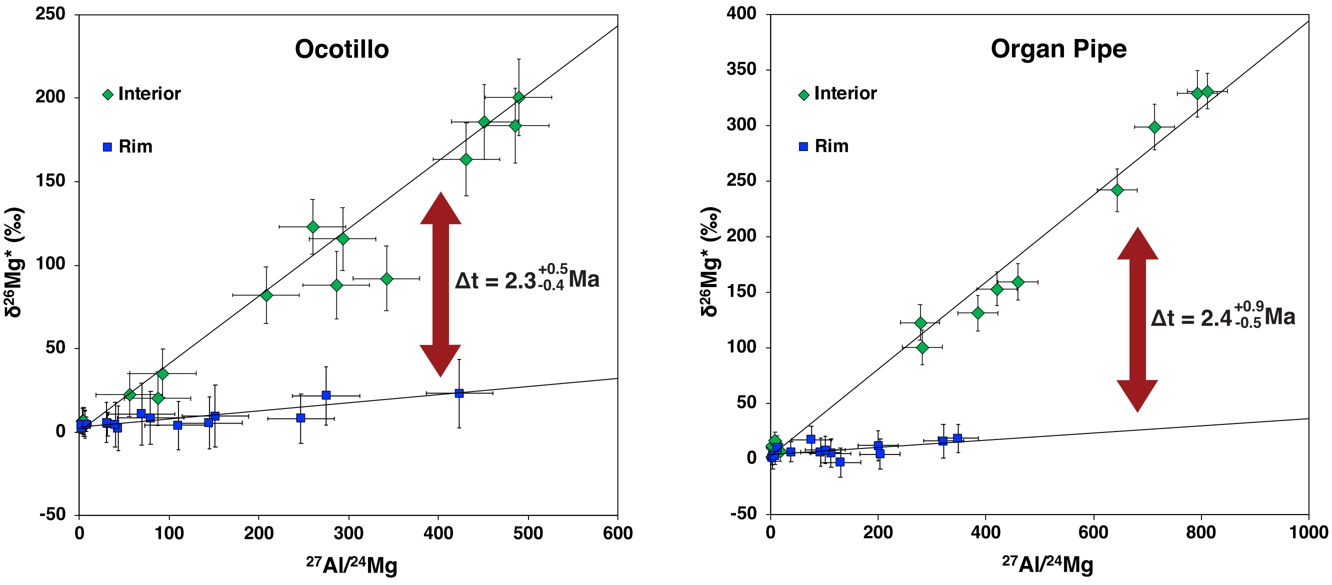

(a) (b)

Figure 2. The ^{26}Al–^{26}Mg systematics in the interior and rim phases of two CAIs (Ocotillo and Organ Pipe) in the NWA 8323 CV3 chondrite. (a) The interior phases in Ocotillo define a slope corresponding to $^{26}\mathrm{Al}/^{27}\mathrm{Al} = (5.2 \pm 0.2) \times 10^{-5}$ and intercept $(\delta^{26}\mathrm{Mg}^{*})_0 = 3.5 \pm 0.8$‰; MSWD = 1.5. The rim phases in this CAI define a slope with $^{26}\mathrm{Al}/^{27}\mathrm{Al}$ ratio $= (5.8 \pm 2.1) \times 10^{-6}$ and intercept $(\delta^{26}\mathrm{Mg}^{*})_0 = 2.9 \pm 0.6$‰; MSWD = 0.26. The relative time difference between the formation (and associated Mg isotope equilibration) of the interior and the rim is $2.3^{+0.5}_{-0.4}$ Ma. (b) The interior phases in Organ Pipe define a slope corresponding to $^{26}\mathrm{Al}/^{27}\mathrm{Al} = (5.3 \pm 0.1) \times 10^{-5}$ and intercept $(\delta^{26}\mathrm{Mg}^{*})_0 = 5.7 \pm 1.4$‰; MSWD = 2.3. The rim phases define a slope with $^{26}\mathrm{Al}/^{27}\mathrm{Al}$ ratio $= (5.5 \pm 1.8) \times 10^{-6}$ and intercept $(\delta^{26}\mathrm{Mg}^{*})_0 = 2.9 \pm 1.1$; MSWD = 0.99. The relative time difference between the formation (and associated Mg isotope equilibration) of the interior and the rim is $2.4^{+0.9}_{-0.5}$ Ma.

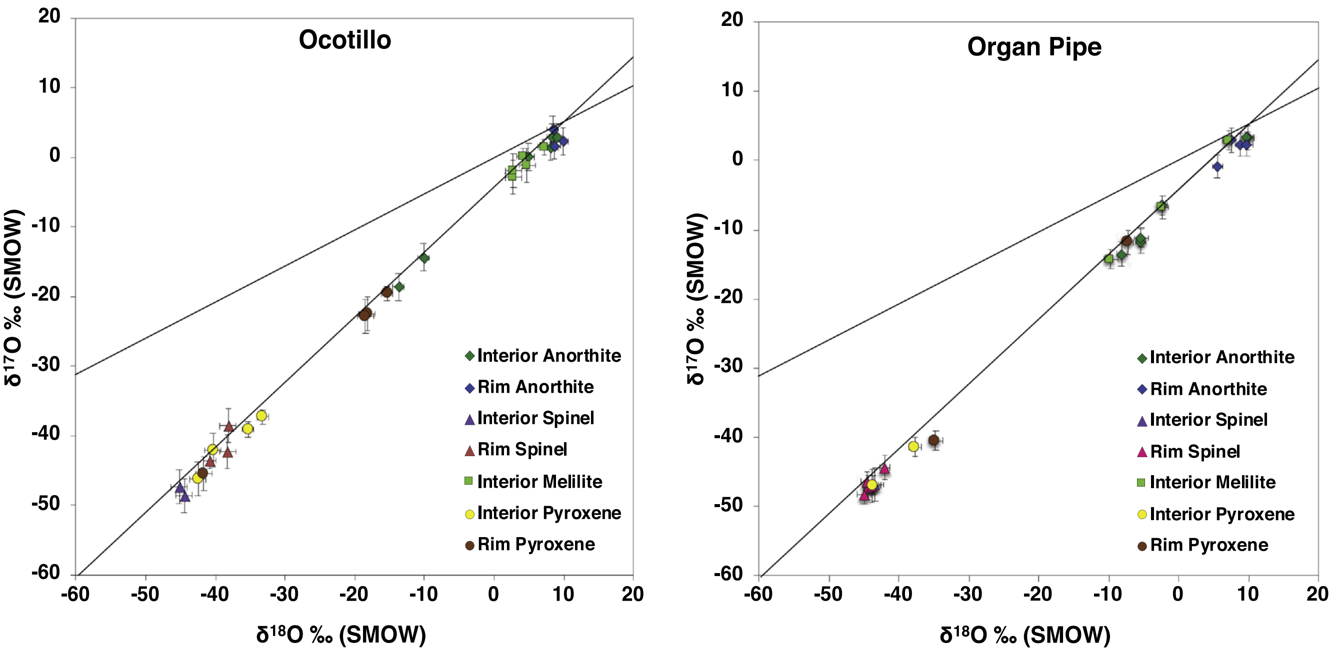

(a) (b)

Figure 3. Oxygen isotopic systematics of mineral phases in the interiors and rims of the (a) Ocotillo and (b) Organ Pipe CAIs.

a result of alteration and replacement of melilite by interaction with ^{16}O-rich gas in a nebular setting (Ushikubo et al. 2017). Similarly, a type B CAI from the Vigarano CV3 reduced carbonaceous chondrite that records a canonical $^{26}\mathrm{Al}/^{27}\mathrm{Al}$ ratio for all its interior phases and most rim phases, also has ^{16}O-rich anorthite that lacks resolvable ^{26}Mg excesses, suggesting late formation of anorthite as a result of alteration and melilite replacement in a nebular setting (Han et al. 2020). However, a type B2 CAI 3529-Z shows abundant coarse-grained anorthite in the mantle just beneath the WL rims (Podosek et al. 1991), similar to the rim anorthite observed in Ocotillo and Organ Pipe. This anorthite layer contains coarse-grained crystals, exhibiting twinning and equant to lath-like habit, which probably formed as a crystallization product from melt and

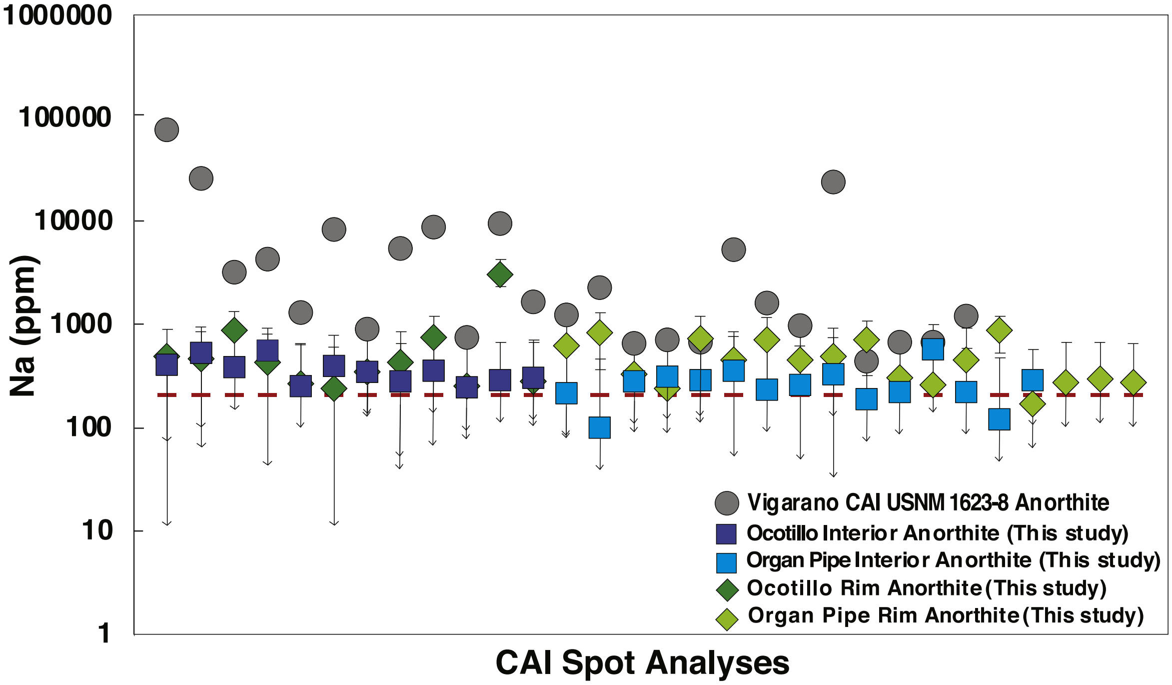

Figure 4. Na abundances in the interior and rim anorthites of Ocotillo and Organ Pipe CAIs. In some cases, only upper limits could be determined and these are indicated as the symbols with the downward pointing arrows. For comparison, the Na abundances in anorthites in a type B CAI from the Vigarano CV3 chondrite (gray circles) are also shown (Macpherson & Davis 1993). The reddashed line is the Na detection limit of the electron microprobe analyses reported in this study.

recorded a lower ^{26}Al/^{27}Al ratio of (1–2) × 10^{-5}. Therefore, this likely suggests formation of the second-generation anorthite at least ~1.5 Ma after the first-generation anorthite in this CAI (Podosek et al. 1991).

The two CAIs analyzed here show only minor evidence of secondary alteration in a parent body setting. The phases analyzed in the interiors of both the CAIs studied here define ^{26}Al–^{26}Mg isochrons with ^{26}Al/^{27}Al ratios that are canonical within the errors (Figure 2), suggesting that they are minimally disturbed in their ^{26}Al–^{26}Mg systematics. There is a possibility that the phases analyzed in the rims, particularly the anorthites, which are characterized by the highest Al/Mg ratios, define isochrons with lower ^{26}Al/^{27}Al ratios because of resetting of the ^{26}Al–^{26}Mg isotopic systematics during secondary alteration. We determined the following geochemical characteristics of the anorthites in particular, as well as oxygen isotope compositions of individual minerals in the interiors and rims of the two CAIs to assess their formation history and whether secondary alteration could have modified the Al–Mg systematics of these CAIs.

4.1.1. Na Abundances

As noted above, anorthite occurs as a primary as well as a secondary alteration phase in CAIs (MacPherson 2014). Correlated analyses of the ^{26}Al–^{26}Mg system and Na abundances of a type B Vigarano CAI USNM 1623-8 show that the coarse-grained anorthite and melilite in this inclusion exhibit elevated Na abundances and no correlation between Al/Mg ratios and ^{26}Mg* excesses (Macpherson & Davis 1993). Given the coarse-grained nature of anorthite in this inclusion, it has been suggested that anorthite was initially formed as a nebular alteration product, which was later melted during a brief heating event, which did not allow all the Na to evaporate (Macpherson & Davis 1993). Compared to the Na abundances reported in the Vigarano CAI USNM 1623-8 (Macpherson & Davis 1993), those measured in the CAI anorthites (in the interior and the rim) in this work are significantly lower (Figure 4). Moreover, unlike USNM 1623-8, the ^{26}Al–^{26}Mg systematics in Ocotillo and Organ Pipe (in the interior as well as the rim) define isochrons with minimal scatter in the data (Figure 2). These ^{26}Al–^{26}Mg systematics combined with the Na abundances in the anorthites in the interiors and rims of Ocotillo and Organ Pipe suggest that the rim anorthites in these two CAIs were likely the result of high-temperature processing in the nebula rather than the product of secondary alteration.

4.1.2. Trace Elemental Abundances

In many CAIs, fine-grained anorthite occurs as an alteration product of melilite (MacPherson 2014). However, alteration products derived from melilite show evidence for loss of Sr (Davis et al. 1994). The abundances of selected trace elements (Eu, Ba, and Sr) were previously reported in two type B CAI from Allende, TS23 and TS24 (Davis et al. 1994). The primary igneous anorthites in these Allende CAIs that show a canonical initial ^{26}Al/^{27}Al ratio have a constant Eu/Sr ratio but a variable Ba/Sr ratio (gray circles in Figure 5). However, alteration products derived from melilite show a positive trend in the plot of Eu/Sr versus Ba/Sr that suggests Sr loss from these phases (pink circles in Figure 5). In comparison, interior as well as rim anorthites from Ocotillo and Organ Pipe show a trend similar to that of primary igneous anorthites in the Allende CAIs, i.e., a constant Eu/Sr ratio but variable Ba/Sr ratio. This suggests that both the interior and rim anorthites in the Ocotillo and Organ Pipe CAIs are igneous in origin and not derived from the secondary alteration of melilite.

4.1.3. Oxygen Isotopic Composition

The following are two possible scenarios that could explain the O isotope variation in individual phases in the interior and rims of the Ocotillo and Organ Pipe CAIs:

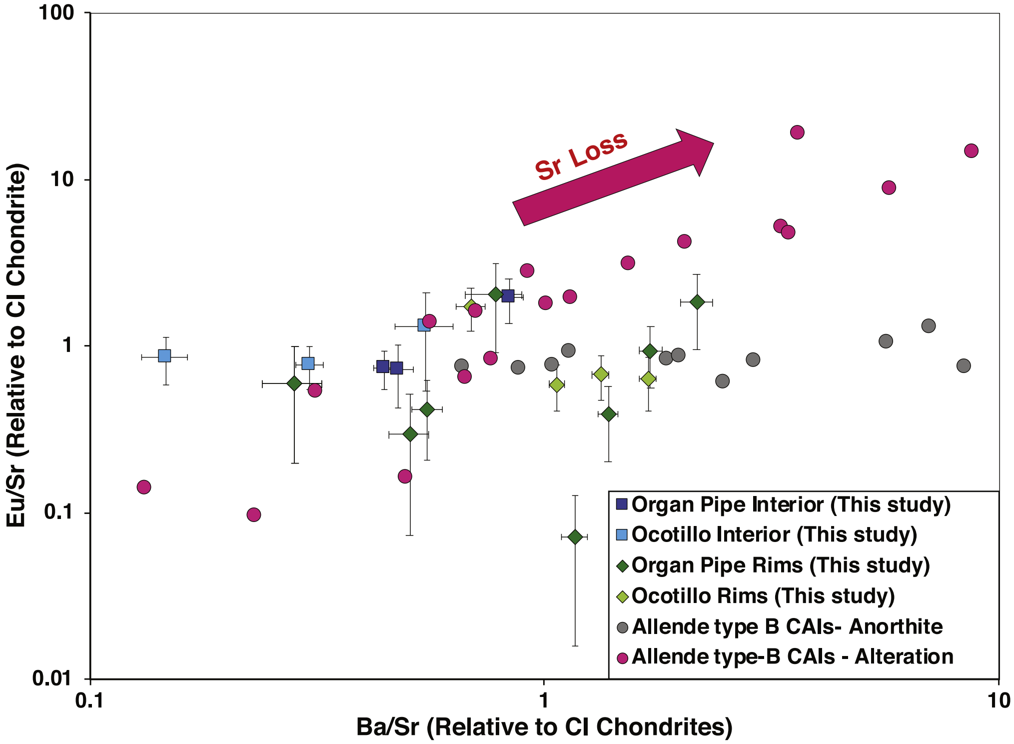

Figure 5. Ba/Sr and Eu/Sr ratios of mineral phases in the interiors and rims of Ocotillo and Organ Pipe CAIs. For comparison, the Ba/Sr and Eu/Sr ratios of undisturbed anorthites and disturbed alteration products from Allende type B CAIs are also shown (Davis et al. 1994).

1. Previous studies (Simon et al. 2011, 2016) have suggested that the exchange of O isotopes with multiple nebular reservoirs (with varying degrees of ^{16}O-enrichment) as the phases in the rim layers crystallized may explain the O isotopic heterogeneity observed in CAI rims. Thus, it is possible that the variation in O isotopes observed in the interior and rim phases of the two CAIs studied here records the O isotope compositions of distinct nebular reservoirs when these phases were forming.
2. Alternatively, the interiors and rims of these CAIs may have originally formed in a ^{16}O-rich nebular environment. In this scenario, secondary alteration (in the nebula or on the parent body) could explain the variation seen in the Ocotillo and Organ Pipe interior and rim phases as resulting from partial O isotope exchange of these phases with a ^{16}O-poor reservoir.

The second scenario is favored over the first one as (i) melilite and anorthite have a high O diffusivity, whereas spinels and pyroxenes are more resistant to O diffusion (Ryerson & McKeegan 1994), and (ii) the melilite and anorthite record the most ^{16}O-poor compositions, while spinels and pyroxenes record the most ^{16}O-rich compositions. In the case of the more likely second scenario described above, the ^{16}O-poor nature of anorthite does not necessarily imply resetting of Mg isotopic composition as O diffuses faster in anorthite compared to melilite (LaTourrette & Wasserburg 1998). This is further supported by the fact that the interior anorthite in both CAIs shows a ^{16}O-poor composition yet has preserved ^{26}Al–^{26}Mg isochrons that record a canonical value for the ^{26}Al/^{27}Al ratio (of ~5.2×10^{-5}; see below) within the errors.

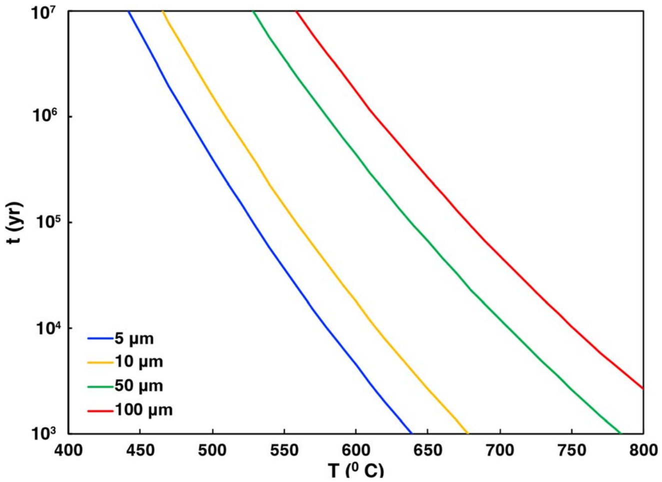

Figure 6. Timescales of equilibration of Mg isotopes in anorthite.

4.2. Implications of the Chronological Data

The phase with the highest Al/Mg ratios in the isochrons shown in Figure 2 (and which controls the slopes of these isochrons) is anorthite. Although coarse-grained anorthite is an igneous mineral in many CAIs (MacPherson 2014), anorthite can also occur as an alteration product of melilite in some CAIs (MacPherson 2014). However, the anorthites in the interiors and rims of Ocotillo and Organ Pipe were likely formed during high-temperature processing in the nebula for following reasons: (1) These anorthites have a coarse-grained texture (Figure 1) characteristic of crystallization from a melt, whereas anorthite produced as an alteration product is typically finer grained (Brearley & Jones 1998); (2) The ^{26}Al–^{26}Mg isotopic data for the interior and rim anorthites in Ocotillo and Organ

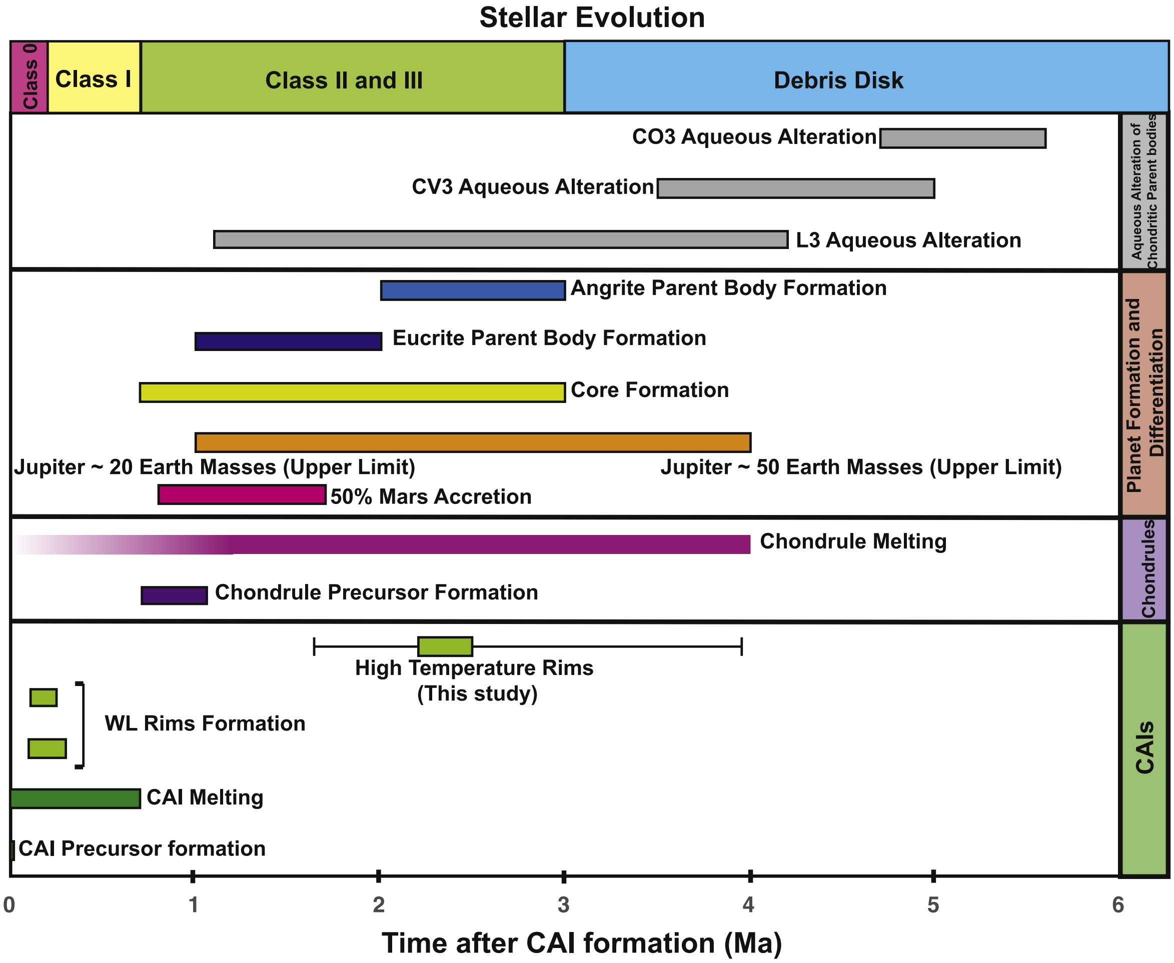

Figure 7. Timescales of early solar system processes in the context of the chronologic data reported here for the interiors and rims of the refractory inclusions, Ocotillo and Organ Pipe, from the NWA 8323 CV3 chondrite. Previously reported data using various chronometers for the timing of early solar system processes are from the following sources: CAI precursor formation (Thrane et al. 2006; Jacobsen et al. 2008); CAI melting (MacPherson et al. 2012); WL rim formation (Simon et al. 2005; Kawasaki et al. 2017); chondrule precursor formation (Villeneuve et al. 2009); chondrule melting (Villeneuve et al. 2009); 50% accretion of Mars (Dauphas & Pourmand 2011); Jupiter formation (Kruijer et al. 2017); planetesimal core formation (Kleine & Wadhwa 2017); Eucrite parent body accretion (Kleine & Wadhwa 2017); Angrite parent body accretion (Kleine & Wadhwa 2017); aqueous alteration of chondritic (L3, CV3, and CO3) parent bodies (Doyle et al. 2015).

Pipe fall along well-correlated linear arrays (Figures 2(a), (b)), where MSWD values for the isochrons for the rim phases are $\leqslant\sim 1$), whereas Al–Mg data for secondary anorthites analyzed in prior studies (e.g., Ito & Messenger 2010) generally show significant scatter; (3) The Na abundances in the anorthites in the interiors and the rims of these CAIs are low (close to or below the detection limit), in contrast with secondary anorthites in CAIs that show significantly elevated Na abundances (e.g., up to a 80,000 ppm Na in secondary anorthites in Vigarano CAIs (Macpherson & Davis 1993; Figure 4)); (4) Finally, the Ba/Sr, and Eu/Sr ratios in anorthites of Ocotillo and Organ Pipe are consistent with a high-temperature origin rather than with their formation by secondary alteration (Figure 5). Specifically, these trace element ratios in anorthites in this study define trends similar to those of unaltered igneous anorthites in Allende CAIs (Davis et al. 1994; Figure 5). Based on these four lines of evidence, we argue that anorthites in the interiors and rims of the Ocotillo and Organ Pipe CAIs have a high-temperature origin in the nebula and that their ^{26}Al–^{26}Mg systematics were not subsequently altered in a parent body setting. Therefore, the relative time difference of ~2–3 Ma reported here between the interiors of each of the two type B CAIs and their respective rims likely represents the time interval between two distinct heating events in the solar nebula. The first heating event melted the precursor CAIs at a time when the ^{26}Al/^{27}Al ratio was close to the canonical value ($\sim 5.2 \times 10^{-5}$; Jacobsen et al. 2008). A subsequent nebular heating event is recorded in the current rims around the CAIs studied here and is required to equilibrate the Al–Mg system in these rims at a later time when the ^{26}Al abundance was an order of magnitude lower.

4.2.1. Potential Equilibration of Mg Isotopes in Rim Anorthite during Parent Body Metamorphism

We estimate the timescales required for the equilibration and homogenization of Mg isotopes in the anorthites analyzed here to assess whether such timescales may be reasonable in the context of parent body alteration. The timescales of Mg equilibration depend on the peak temperatures experienced by the meteorite during thermal metamorphism. Allende is one of the most widely studied CV3 meteorites. Raman spectroscopic analysis of insoluble organic matter suggests a peak temperature of up to ~624°C for this chondrite (Bose et al. 2017), whereas Mg diffusion in anorthites in Allende CAIs suggests a peak metamorphic temperature of ~600°C (Ito & Messenger 2010). Overall, however, the estimates for the peak temperature for the Allende parent body vary significantly; these range from 300°C–830°C, as estimated by various methods such as noble gas measurements in presolar nanodiamonds, Fe–Mg zoning in chondrule olivine, and petrographic observations (Weinbruch et al. 1990; Cuvillier et al. 2015). Different CV3 meteorites are estimated to have experienced different peak metamorphic temperatures. Based on the confocal imaging of insoluble organic matter using Raman spectroscopy, estimates for the peak metamorphic temperatures vary between 260°C and 590°C (Busemann et al. 2007).

We used an approach similar to that described in LaTourrette & Wasserburg (1998) to estimate the timescales of isotopic homogenization. Isotopic homogenization is defined as having occurred when 90% of Mg has been exchanged with the surroundings. Both the interior and rim anorthite are surrounded by relatively Mg-rich phases such as melilite, spinel, and pyroxene.

For these conditions, the isotopic homogenization should satisfy the following equation:

$$Dt/a^2 = 0.25,$$

where D is the diffusion coefficient for Mg in anorthite at a given temperature, t is the time required for the equilibration and a is the radius of the crystal. The diffusion coefficient D is determined from the Arrhenius equation:

$$D = D_0 e^{(-E/RT)},$$

where $D_0 = 7.1 \times 10^{-8}\ \mathrm{m^2\ s^{-1}}$, $E = 254 \pm 43\ \mathrm{kJ\ mol^{-1}}$ (values from LaTourrette & Wasserburg 1998), R is the gas constant ($8.314\ \mathrm{J\,K^{-1}\,mol}$), and T is temperature. Similar diffusion calculations can be applied to O diffusion in anorthite, where $D_0 = 8.4 \times 10^{-13}\ \mathrm{m^2\ s^{-1}}$, $E = 162 \pm 36\ \mathrm{kJ\ mol^{-1}}$ (values from Ryerson & McKeegan 1994).

Our isothermal diffusion calculations are consistent with those of LaTourrette & Wasserburg (1998), and suggest that effectively no Mg isotopic exchange will occur below 450°C, while the largest anorthite crystals will homogenize within 100,000 yr at 750°C (Figure 6). Given that the grain size of the rim anorthite is 10–20 μm, we estimate that for an anorthite crystal with $a = 5\ \mu$m, it would take ~0.4 million yr to reset its Mg isotopic composition at an equilibration temperature of 500°C, whereas at 550°C, Mg isotopic homogenization would take only a few tens of thousands of years (Figure 6). For the coarser-grained interior anorthite, we consider $a = 50\ \mu$m; for such an anorthite, Mg isotopic equilibration at 500°C would take ~40 million yr, but could be achieved within a million years at 600°C (Figure 6). Both the interior and rim anorthites in these CAIs show partial to complete exchange of O isotopes with the ^{16}O-poor reservoir. If we assumed that the O isotopic equilibration occurred during parent body metamorphism, then for a peak metamorphic temperature of 550°C an anorthite crystal of $a = 50\ \mu$m will experience O isotopic equilibration in ~0.5 million yr, whereas at ~500°C such a crystal would require over a million years for O isotopic homogenization.

The duration of parent body metamorphism recorded in a meteoritic sample depends on the size of that parent body and the depth of burial of that sample. These parameters are not well constrained for the NWA 8323 CV3 chondrite. As such, we make a simplified assumption that the peak metamorphic temperatures lasted for 0.5–1 million yr for the CAIs from this meteorite. Therefore, if a peak metamorphic temperature of ~550°C was sustained for such a duration, for NWA 8323, it would be possible to reset the O isotopic composition of both the interior and rim anorthite as well as Mg isotopic composition of rim anorthites, while preserving the Mg isotopic composition of interior anorthites in the two CAIs studied here.

The peak metamorphic temperature for NWA 8323 has not yet been determined. Given the range of estimates of the peak metamorphic temperatures for other CV3 chondrites from previous studies, it may be possible that NWA 8323 experienced a peak metamorphic temperature of ~550°C for about a million years or so, such that the Mg isotopic composition of the rim anorthite in the two CAIs studied here were reset within a short (sub-Ma) timescale while the Mg isotopic composition of the interior anorthite was preserved (and O isotopes in both the rim and interior anorthite were disturbed). Nonetheless, given the large range of estimates of peak temperatures experienced by CV3 meteorites and without an independent determination of the temperatures and duration of metamorphism experienced by NWA 8323, such calculations of diffusion timescales remain inconclusive. Based on the petrology, trace elemental abundances, and the goodness of fit of the ^{26}Al isochrons discussed in Section 4.1, it seems unlikely that the Mg isotopes in the rim anorthite in the two CAIs studied here were disturbed during the meteorite parent body metamorphism. Indeed, based on the calculations shown here, if NWA 8323 experienced a peak metamorphic temperature of less than ~550°C for a duration of about 0.5 million yr or less, it is possible that Mg isotopes were preserved in the rim anorthites.

4.2.2. Potential ^{26}Al Heterogeneity in the Early Solar System

For the ^{26}Al–^{26}Mg system to yield meaningful chronological information, ^{26}Al must be homogenously distributed in the early solar system. Many previous studies have argued for a homogeneous distribution of ^{26}Al at least in the CAI-forming region of the solar nebula, with a canonical value for the ^{26}Al/^{27}Al ratio of $\sim 5.2 \times 10^{-5}$ at the time of CAI formation (Jacobsen et al. 2008; Kita et al. 2013; Kruijer et al. 2014; Budde et al. 2018; Pignatale et al. 2019). However, some recent studies have challenged the assumption of ^{26}Al homogeneity given the apparent discordance between different chronometers while dating chondritic components (e.g., Connelly et al. 2012; Bollard et al. 2017, 2019) as well as differentiated meteorites (e.g., Schiller et al. 2015; Larsen et al. 2016). Nevertheless, a potential cause of this discordance could be that secondary processes may affect some chronometers to a greater extent than others.

In this study, we have focused on determining the relative difference in the timing of the last equilibration of the Al–Mg system between the interior and the rim of each CAI. As such, if the Al–Mg system in these CAIs (interiors and rims) remained as a closed system, the issue of ^{26}Al heterogeneity would be irrelevant to the determination of the chronology of the rim relative to the interior. However, if rim formation in these CAIs did not occur as a closed system, and if the rims exchanged material with the nebular gas, then it would indeed be important that ^{26}Al be homogeneously distributed in the reservoir in which these CAIs and their rims formed. The ^{26}Al homogeneity is well established in the CAI-forming region by comparing various chronometers (Thrane et al. 2006; Jacobsen et al. 2008; Kita et al. 2013; Kruijer et al. 2014). As discussed earlier, the ranges in the oxygen isotopic compositions of the phases in the interiors and rims of the two CAIs studied here favor the scenario wherein they originally formed in a similar (^{16}O-rich) nebular environment. Therefore, it seems reasonable to assume ^{26}Al homogeneity is the nebular reservoir in which these CAI hosts and their rims formed.

4.3. Formation History of the Ocotillo and Organ Pipe CAIs

Based on the petrography of the CAIs, as well as their trace elemental and O isotopic data presented in this study, the most likely scenario for the formation of the Ocotillo and Organ Pipe CAIs and their rim sequences involves at least the following stages:

1. Formation of precursors of these CAIs by condensation and accretion.
2. A transient heating event that melted these precursors and formed the coarse-grained igneous textures currently observed in the interiors of the Ocotillo and Organ Pipe CAIs and recorded a canonical $^{26}\mathrm{Al}/^{27}\mathrm{Al}$ ratio (i.e., $\sim 5 \times 10^{-5}$; defining $t = 0$).
3. It is possible (although not certain) that typical WL rims formed around these CAIs during a time interval $\Delta t = \sim 0 - \sim 300$ ka relative to the formation of the CAI interiors. This is based on previous studies of WL rims around other CAIs that have shown that those rims were formed within this time interval (Simon et al. 2005; Kawasaki et al. 2017; Han et al. 2020). Furthermore, the melilite in these more typical WL rims may have been altered to anorthite in a nebular environment.
4. A subsequent nebular heating event produced the currently observed rims around these two CAIs (this event would have remelted any original WL rims if they were formed as noted in stage 3 above) at a time when the $^{26}\mathrm{Al}/^{27}\mathrm{Al}$ ratio had decayed and was reduced by an order of magnitude compared to the canonical value (i.e., ∼2–3 Ma after the formation of the interior of these CAIs). The rim isochrons are primarily defined by the anorthite which shows textural and chemical evidence of being flash-heated and melted. Nonetheless, it is possible that the spinel and pyroxene formed by other mechanisms after this melting event.
5. It is noted that if the formation of secondary anorthite (possibly from the replacement of primary melilite) took place (stage 3 above), it would likely contain significant Na and would likely show evidence for loss of Sr. As discussed previously in Sections 4.1.1 and 4.1.2 above, neither of these characteristics is observed in the rim anorthites in Ocotillo and Organ Pipe. During the subsequent melting event (stage 4 above), it is possible that most of the Na and other volatiles evaporated resulting in the low abundances reported here (Figure 4). Such a melting process could potentially also homogenize the Sr abundances, such that these anorthites would not show the Sr loss trend (Figure 5). In fact, evidence of nebular alteration of CAIs has been reported previously by Fagan et al. (2007). However, any signatures of such an earlier alteration of the Ocotillo and Organ Pipe CAIs had to have been erased during the subsequent melting event (stage 4 above) that occurred ∼2–3 Ma after the original melting event when the ^{26}Al abundance was near canonical (stage 2 above).
6. Accretion of these CAIs on the CV3 parent body.

There is a possibility of minor alteration of Ocotillo and Organ Pipe in a parent body setting given the Fe-rich nature of some rim spinel and some occurrence of hedenbergite (FeO-rich pyroxene) in the rim pyroxene layer (see Appendix A, Tables 6 and 7 for major element compositions of these phases). However, all the rim spinel grains (including the FeO-rich grains) show ^{16}O-rich oxygen isotopic compositions (Figure 3), which indicates that at least their O isotopes were not significantly affected by parent body alteration. The outermost pyroxene layer has a finer grain size compared to the rim anorthites and spinels and shows some occurrence of FeO-rich pyroxene. Pyroxenes in this layer have an O isotopic composition that is not as ^{16}O-rich as the rim spinels, but more ^{16}O-rich than the rim anorthites. However, the fine grain size of the rim pyroxenes makes analysis with the electron microprobe (for determining Fe content) and secondary ion mass spectrometer (for measuring O isotopes) more challenging than for the rim anorthites and spinels. It is possible that the Fe-rich nature and O isotopic composition of the rim pyroxene is the result of beam overlap on multiple grains or phases (perhaps including some meteorite matrix) during analyses. Nevertheless, as discussed earlier, the rim anorthites (which have the highest Al/Mg ratios among the phases analyzed in the rims of the CAIs Ocotillo and Organ Pipe, and determine the slopes of the Al–Mg isochrons for these rims shown in Figure 2) do not show any significant mineralogical, chemical, or isotopic evidence of secondary alteration.

4.4. Astrophysical Significance of Protracted Nebular Processing of CAIs

Previous studies of ^{26}Al–^{26}Mg systematics in refractory inclusions imply that the precursor materials of CAIs formed during a short time interval of $\leqslant$20 ka in the early solar system (Jacobsen et al. 2008; Figure 7); subsequent melting and remelting episodes continued for at least another ∼0.2 Ma (Hsu et al. 2000; MacPherson et al. 2010), and possibly up to ∼0.7 Ma for some CAIs (MacPherson et al. 2012). The results presented here suggest that the melting of some CAI rim layers extended for up to ∼2–3 Ma (Figure 7). Our chronologic and other geochemical data from two CAI interiors and rims indicate this extended duration of time for these objects to have remained free-floating in the solar nebula.

Chondrules may have formed almost contemporaneously with the first solids in the solar nebula (Connelly et al. 2012; Bollard et al. 2017, 2019). Their melting and remelting are argued to have occurred in transient heating events such as gravitational instabilities-driven shocks or planetesimal bow shocks (Desch et al. 2012) for up to ∼4 Ma thereafter (Villeneuve et al. 2009). Given that CAIs appear to have experienced melting in the solar nebula over a similar time period, from close to the time of original CAI formation (Hsu et al. 2000; Simon et al. 2005; MacPherson et al. 2010, 2012; Kawasaki et al. 2017) to ∼2–3 Ma thereafter (this study), similar heating mechanisms may be responsible for the thermal processing of both CAIs and chondrules in the solar nebula, albeit in spatially distinct regions with different chemical and isotopic characteristics (Krot et al. 2002; Grossman et al. 2008; Yurimoto et al. 2008). Astrophysical mechanisms proposed to explain the melting of igneous CAIs, including FU Orionis outbursts, Exor outbursts, and X-ray flares, operate over the duration of months to 10^3–10^5 yr (Connolly et al. 2006). However, partial melting of CAIs to produce rims such as those observed on the Ocotillo and Organ Pipe CAIs requires mechanisms that would produce peak heating over much shorter timescales in the solar nebula (such that only the exteriors of the CAIs are remelted while the interiors remain unaffected). As such, short-duration nebular shocks, such as those responsible for melting chondrules may be responsible for partially melting these CAIs as well.

The survival of CAI-sized solids in a nonturbulent solar nebula for a few Ma after their formation is difficult because the inward radial drift due to gas drag is expected to accrete CAIs onto the Sun within $\sim 10^6$ yr (Weidenschilling 1977; Cuzzi & Weidenschilling 2006). Indeed, it was thought that one way for such objects to survive was to store them in a first generation of early-formed planetesimals that were later disrupted and then re-accreted with chondrules to form chondrites (Weidenschilling et al. 1998). However, this is problematic because to prevent the loss of such bodies via gas drag, they needed to be >1 km in size, and such large bodies would undergo melting after early accretion with a near-canonical abundance of ^{26}Al. Thereafter, it was suggested that turbulence can cause CAI-sized particles to drift outward to asteroidal distances and could allow them to survive for 1–3 Ma (Cuzzi et al. 2003). Another mechanism proposed to explain the outward movement of refractory inclusions is a viscous expansion of the protoplanetary disk in its earliest stages ($<10^5$ yr; Ciesla 2010), which could carry CAIs to large heliocentric distances. Gaseous motions associated with spiral arms in a marginally gravitationally unstable disk may also preserve and transport CAIs in the outward direction (Boss 2008), thereby preventing them from spiraling inward into the Sun. The recent Atacama Large Millimeter/submillimeter Array images of other protoplanetary disks show structures, spiral arms, and gaps in the disks, suggesting that heterogeneous mass transport and possible pressure bumps could prevent CAIs from being accreted onto the Sun (e.g., Benisty et al. 2015). It was proposed recently that the formation of Jupiter's core (i.e., up to 30 Earth masses) at ∼0.6 Ma after solar system formation may have opened a gap in the nebular disk such that early-formed CAIs were trapped in the pressure maximum just beyond Jupiter (Desch et al. 2018). These trapped CAIs could have remained free-floating (and subject to subsequent nebular heating events) until they were accreted onto their parent bodies a few million years thereafter. These astrophysical scenarios all seem to require CAIs to be transported outwards soon after their formation. If they were transported out to chondrule-forming regions, it raises questions about why most CAIs do not appear to show evidence for thermal processing beyond ∼1 Ma after solar system formation (as chondrules clearly do). Our results reported here imply that the duration of thermal processing of CAIs did indeed extend up to ∼2–3 Ma after the solar system formation.

In summary, the results reported here are consistent with the suggestion that most CAIs were initially formed during a brief time period (when the ^{26}Al/^{27}Al ratio was near canonical); our data additionally demonstrate that some of these CAIs were thermally processed in a nebular environment up to ∼2–3 Ma later, i.e., during the classical T Tauri phase (Class II phase) of the stellar evolution (Figure 7). Meteoritical data indicate that planetesimal accretion and differentiation occurred early, beginning within ∼1 Ma of the formation of the earliest-formed solids in the solar system (i.e., CAIs; Kleine & Wadhwa 2017). Isotopic evidence suggests that Mars accreted ∼50% of its current mass within the first ∼2 Ma after CAI formation (Dauphas & Pourmand 2011) and Jupiter's core grew to at least 20 Earth masses within ∼1 Ma and up to 50 Earth masses within ∼3–4 Ma following CAI formation (Kruijer et al. 2017; Figure 7). Taken together, meteoritical data suggest that planetesimal accretion occurred quickly and that planetary embryos (i.e., at least half the size of Mars and possibly larger) existed while smaller solids, like chondrules and CAIs, were being thermally processed in the solar nebula. Previous studies have suggested that nebular shocks such as gravitational instabilities-driven shocks or planetary bow shocks are the likely mechanisms for chondrule formation (Desch et al. 2012). Given that the ages of the CAI rims analyzed here are contemporaneous with chondrule formation as well as planetesimal formation, this may support the hypothesis that early-accreted bodies created bow shocks (Hood et al. 2009) or gravitational instabilities-driven shocks (if the accreted bodies were large enough; Boss & Durisen 2005) to provide a heating mechanism in the solar nebula. Furthermore, such a heating mechanism need not be spatially restricted, i.e., to just the chondrule-forming region(s). The results reported here additionally bolster recent evidence (e.g., Kleine et al. 2005; Kleine & Wadhwa 2017) for chondritic materials accreting later than the early-formed planetary embryos, indicating that the components of chondrites (including CAIs, along with their high-temperature rims, as well as chondrules) were accreted relatively late to form chondritic parent bodies after ^{26}Al, the primary heat source for differentiation of early-formed rocky bodies most likely, had mostly decayed away.

We thank the Center for Meteorite Studies at Arizona State University for loaning the NWA 8323 meteorite sample. We thank Dr. Ken Domanik for his assistance with the electron microprobe, Dr. Noriko Kita for her assistance in acquiring oxygen isotopic data, Dr. Glenn MacPherson for his assistance with the SEM analyses and many useful discussions, and CAMECA engineers Jianchao Zhang and David Haugan for their advice on NanoSIMS data reduction for this manuscript. This work was supported by a NASA Earth and Space Science Fellowship (NNX13AP41H) to P.M. and M.W. and grants from the NASA Cosmochemistry (NNX11AK75G) and Emerging Worlds (NNX15AH41G) programs to M.W. M.B. was supported in part by the Nexus for Exoplanet System Science (NExSS) grant (NNX15AD94G) and the NSF facility grant (EAR-1352996). The authors would like to thank the editor Faith Vilas and three anonymous reviewers for their feedback in the review process. This paper is LPI Contribution No. 2872. LPI is operated by USRA under a cooperative agreement with the Science Mission Directorate of the National Aeronautics and Space Administration.

Appendix A
Elemental Composition of CAIs

Here we report oxide weight percentage of major elements measured using EPMA and the calculated atomic number per formula unit for major mineral phases in the Ocotillo and Organ Pipe CAIs (Tables 6–7).

Table 6

Elemental Composition of Mineral Phases in Ocotillo

	Oxides wt%											Atomic Number per Formula Unit											
	MgO	Na_2O	SiO_2	Al_2O_3	CaO	FeO	K_2O	Cr_2O_3	TiO_2	MnO	Total	Mg	Na	Si	Al	Ca	Fe	K	Cr	Ti	Mn	Total[a]	Åk Content
Interior anorthite-1	0.04	0.06	42.58	37.23	20.20	0.07	b.d.*	0.01	0.06	b.d.*	100.24	0.00	0.01	1.97	2.03	1.00	0.00	⋯	0.00	0.00	⋯	5.02(8)	⋯
Interior anorthite-2	0.08	0.07	43.18	37.46	20.23	0.05	b.d.*	0.02	0.06	b.d.*	101.15	0.01	0.01	1.98	2.02	0.99	0.00	⋯	0.00	0.00	⋯	5.01(8)	⋯
Interior anorthite-3	0.02	0.05	43.15	37.47	20.22	0.11	0.01	b.d.*	0.05	b.d.*	101.09	0.00	0.00	1.98	2.03	0.99	0.00	0.00	⋯	0.00	⋯	5.01(8)	⋯
Interior anorthite-4	0.08	0.08	43.19	37.34	20.11	0.00	b.d.*	0.01	0.06	b.d.*	100.88	0.01	0.01	1.98	2.02	0.99	0.00	⋯	0.00	0.00	⋯	5.01(8)	⋯
Interior anorthite-5	0.02	0.04	42.65	37.35	20.20	0.08	b.d.*	0.01	0.07	b.d.*	100.40	0.00	0.00	1.97	2.03	1.00	0.00	⋯	0.00	0.00	⋯	5.01(8)	⋯
Interior anorthite-6	0.07	0.06	43.06	37.42	20.27	0.10	b.d.*	b.d.*	0.07	b.d.*	101.04	0.00	0.00	1.98	2.02	1.00	0.00	⋯	⋯	0.00	⋯	5.01(8)	⋯
Interior anorthite-7	0.17	0.05	42.73	37.51	20.17	0.01	b.d.*	b.d.*	0.05	0.02	100.72	0.01	0.00	1.97	2.04	0.99	0.00	⋯	⋯	0.00	0.00	5.02(8)	⋯
Interior anorthite-8	0.15	0.04	42.74	37.22	20.17	0.04	b.d.*	b.d.*	0.08	0.04	100.48	0.01	0.00	1.97	2.02	1.00	0.00	⋯	⋯	0.00	0.00	5.01(8)	⋯
Interior anorthite-9	0.09	0.05	42.99	37.19	20.17	0.01	b.d.*	0.01	0.06	b.d.*	100.58	0.01	0.00	1.98	2.02	1.00	0.00	⋯	0.00	0.00	⋯	5.01(8)	⋯
Interior anorthite-10	0.05	0.03	42.70	37.21	20.26	b.d.*	b.d.*	b.d.*	0.10	b.d.*	100.36	0.00	0.00	1.97	2.03	1.00	0.00	⋯	⋯	0.00	⋯	5.01(8)	⋯
Interior anorthite-11	0.11	0.04	42.90	37.09	20.19	0.04	0.01	b.d.*	0.09	b.d.*	100.48	0.01	0.00	1.98	2.02	1.00	0.00	0.00	⋯	0.00	⋯	5.01(8)	⋯
Interior anorthite-12	0.05	0.04	42.78	37.17	20.18	b.d.*	0.01	0.02	0.06	b.d.*	100.32	0.00	0.00	1.98	2.02	1.00	0.00	0.00	0.00	0.00	⋯	5.01(8)	⋯
Rim anorthite-1	0.61	0.07	41.98	36.65	20.43	0.24	b.d.*	0.01	0.03	b.d.*	100.01	0.04	0.01	1.95	2.01	1.02	0.01	⋯	0.00	0.00	⋯	5.04(8)	⋯
Rim anorthite-2	0.34	0.06	42.78	37.33	19.98	0.23	b.d.*	b.d.*	0.02	0.03	100.79	0.02	0.01	1.97	2.03	0.99	0.01	⋯	⋯	0.00	0.00	5.02(8)	⋯
Rim anorthite-3	0.26	0.12	43.15	37.08	19.52	0.31	0.01	b.d.*	b.d*	b.d.*	100.46	0.02	0.01	1.99	2.01	0.96	0.01	0.00	⋯	0.00	⋯	5.01(8)	⋯
Rim anorthite-4	0.29	0.06	43.28	37.25	19.75	0.24	0.01	0.01	0.02	b.d.*	100.89	0.02	0.01	1.99	2.01	0.97	0.01	0.00	0.00	0.00	⋯	5.01(8)	⋯
Rim anorthite-5	0.21	0.04	42.69	37.31	20.30	0.33	b.d.*	0.01	0.01	b.d.*	100.89	0.01	0.00	1.97	2.02	1.00	0.01	⋯	0.00	0.00	⋯	5.02(8)	⋯
Rim anorthite-6	0.04	0.03	42.24	37.16	20.12	0.27	b.d.*	0.01	0.01	b.d.*	99.88	0.00	0.00	1.96	2.04	1.00	0.01	⋯	0.00	0.00	⋯	5.02(8)	⋯
Rim anorthite-7	1.42	0.05	40.25	39.05	19.10	0.69	b.d.*	0.01	0.23	b.d.*	100.83	0.10	0.00	1.86	2.13	0.95	0.03	⋯	0.00	0.01	⋯	5.07(8)	⋯
Rim anorthite-8	0.35	0.06	42.13	37.67	20.01	0.42	b.d.*	b.d.*	0.03	b.d.*	100.67	0.02	0.01	1.95	2.05	0.99	0.02	⋯	⋯	0.00	⋯	5.03(8)	⋯
Rim anorthite-9	0.26	0.10	42.08	37.48	20.21	0.35	0.01	0.01	0.02	0.02	100.55	0.02	0.01	1.95	2.04	1.00	0.01	0.00	0.00	0.00	0.00	5.04(8)	⋯
Rim anorthite-10	0.01	0.04	42.50	37.31	19.94	0.19	b.d.*	0.01	0.08	b.d.*	100.07	0.00	0.00	1.97	2.04	0.99	0.01	⋯	0.00	0.00	⋯	5.01(8)	⋯
Rim anorthite-11	0.23	0.43	42.92	36.89	19.22	0.32	0.01	b.d.*	0.06	0.02	100.10	0.02	0.04	1.99	2.01	0.95	0.01	0.00	⋯	0.00	0.00	5.02(8)	⋯
Rim anorthite-12	b.d.*	0.04	42.15	37.21	20.11	0.21	0.01	b.d.*	0.10	0.02	99.85	0.00	0.00	1.96	2.04	1.00	0.01	0.00	⋯	0.00	0.00	5.02(8)	⋯
Interior spinel-1	27.67	b.d.*	0.07	71.09	0.23	0.07	b.d.*	0.30	0.67	0.02	100.12	0.98	⋯	0.00	1.99	0.01	0.00	⋯	0.01	0.01	0.00	2.99(4)	⋯
Interior spinel-2	27.64	0.01	0.10	71.61	0.17	0.09	b.d.*	0.33	0.32	b.d.*	100.25	0.97	0.00	0.00	2.00	0.00	0.00	⋯	0.01	0.01	⋯	2.99(4)	⋯
Interior spinel-3	28.01	b.d.*	0.03	71.93	0.06	0.02	b.d.*	0.13	0.29	b.d.*	100.47	0.98	⋯	0.00	2.00	0.00	0.00	⋯	0.00	0.01	⋯	2.99(4)	⋯
Interior spinel-4	27.92	b.d.*	0.01	72.00	0.02	0.08	b.d.*	0.16	0.32	b.d.*	100.52	0.98	⋯	0.00	2.00	0.00	0.00	⋯	0.00	0.01	⋯	2.99(4)	⋯
Interior spinel-5	27.59	b.d.*	0.04	71.96	0.03	0.01	b.d.*	0.18	0.29	b.d.*	100.11	0.97	⋯	0.00	2.01	0.00	0.00	⋯	0.00	0.01	⋯	2.99(4)	⋯
Interior spinel-6	28.00	b.d.*	0.03	71.75	0.04	0.03	b.d.*	0.21	0.25	b.d.*	100.31	0.99	⋯	0.00	2.00	0.00	0.00	⋯	0.00	0.00	⋯	2.99(4)	⋯
Interior spinel-7	27.79	0.01	0.06	71.60	0.04	0.03	b.d.*	0.19	0.25	b.d.*	99.97	0.98	0.00	0.00	2.00	0.00	0.00	⋯	0.00	0.00	⋯	2.99(4)	⋯
Interior spinel-8	27.88	b.d.*	0.03	72.04	0.06	b.d.*	b.d.*	0.14	0.32	b.d.*	100.49	0.98	⋯	0.00	2.00	0.00	0.00	⋯	0.00	0.01	⋯	2.99(4)	⋯
Interior spinel -9	27.58	b.d.*	0.07	71.43	0.15	0.01	0.01	0.28	0.16	0.01	99.70	0.98	⋯	0.00	2.00	0.00	0.00	0.00	0.01	0.00	0.00	2.99(4)	⋯
Rim spinel-1	25.33	0.01	1.77	68.27	0.79	3.72	b.d.*	0.34	0.22	0.02	100.46	0.91	0.00	0.04	1.93	0.02	0.07	⋯	0.01	0.00	0.00	2.99(4)	⋯
Rim spinel-2	24.72	0.01	3.39	66.69	1.25	3.65	0.01	0.32	0.45	b.d.*	100.48	0.88	0.00	0.08	1.88	0.03	0.07	0.00	0.01	0.01	⋯	2.97(4)	⋯
Rim spinel-3	25.15	b.d.*	0.42	69.59	0.20	4.46	b.d.*	0.28	0.20	0.02	100.32	0.90	⋯	0.01	1.98	0.01	0.09	⋯	0.01	0.00	0.00	3.00(4)	⋯
Rim spinel-4	26.28	b.d.*	0.36	70.89	0.32	2.52	b.d.*	0.22	0.24	0.02	100.86	0.93	⋯	0.01	1.99	0.01	0.05	⋯	0.00	0.00	0.00	2.99(4)	⋯
Rim spinel-5	26.44	b.d.*	0.95	70.45	0.60	1.83	b.d.*	0.24	0.28	b.d.*	100.79	0.93	⋯	0.02	1.97	0.02	0.04	⋯	0.00	0.01	⋯	2.99(4)	⋯
Rim spinel-6	27.40	0.01	0.15	71.51	0.18	1.45	b.d.*	0.19	0.23	0.02	101.14	0.96	0.00	0.00	1.99	0.00	0.03	⋯	0.00	0.00	0.00	3.00(4)	⋯
Rim spinel-7	27.26	b.d.*	0.20	71.25	0.26	1.36	b.d.*	0.17	0.23	0.02	100.76	0.96	⋯	0.00	1.99	0.01	0.03	⋯	0.00	0.00	0.00	3.00(4)	⋯
Interior pyroxene-1	5.47	b.d.*	29.59	25.06	24.38	0.01	b.d.*	0.11	14.84	b.d.*	99.47	0.31	⋯	1.11	1.11	0.98	0.00	⋯	0.00	0.42	⋯	3.92(6)	⋯
Interior pyroxene-2	5.53	b.d.*	30.38	24.26	24.59	0.01	b.d.*	0.12	14.11	b.d.*	99.01	0.31	⋯	1.14	1.07	0.99	0.00	⋯	0.00	0.40	⋯	3.92(6)	⋯
Interior pyroxene-3	6.01	b.d.*	31.52	24.26	24.54	0.04	0.01	0.11	13.06	0.01	99.56	0.33	⋯	1.17	1.07	0.98	0.00	0.00	0.00	0.37	0.00	3.92(6)	⋯
Interior pyroxene-4	7.63	b.d.*	34.77	21.82	24.84	b.d.*	b.d.*	0.10	10.28	b.d.*	99.44	0.42	⋯	1.29	0.95	0.99	⋯	⋯	0.00	0.29	⋯	3.94(6)	⋯
Interior pyroxene-5	7.94	b.d.*	35.42	21.49	24.68	b.d.*	b.d.*	0.10	9.80	b.d.*	99.43	0.44	⋯	1.31	0.94	0.98	⋯	⋯	0.00	0.27	⋯	3.94(6)	⋯
Interior pyroxene-6	9.12	b.d.*	37.53	18.67	24.89	b.d.*	b.d.*	0.08	9.40	b.d.*	99.71	0.50	⋯	1.39	0.81	0.98	⋯	⋯	0.00	0.26	⋯	3.95(6)	⋯
Interior pyroxene-7	8.71	0.02	36.65	18.57	24.88	0.03	b.d.*	0.11	10.10	b.d.*	99.07	0.48	0.00	1.36	0.82	0.99	0.00	⋯	0.00	0.28	⋯	3.94(6)	⋯
Interior pyroxene-8	7.13	b.d.*	33.65	22.06	24.61	0.01	0.01	0.11	11.31	0.02	98.92	0.40	b.d.	1.26	0.97	0.99	0.00	0.00	0.00	0.32	0.00	3.94(6)	⋯
Interior pyroxene-9	3.16	b.d.*	39.43	22.95	34.50	0.03	b.d.*	b.d*	0.02	b.d.*	100.10	0.18	b.d.	1.47	1.01	1.38	0.00	b.d.	0.00	0.00	b.d.	4.03(6)	⋯
Interior pyroxene-10	8.65	0.01	36.67	18.89	24.76	0.03	b.d.*	0.09	9.87	0.01	98.98	0.48	0.00	1.37	0.83	0.99	0.00	⋯	0.00	0.28	0.00	3.94(6)	⋯
Interior pyroxene-11	7.54	b.d.*	34.78	21.80	24.69	b.d.*	0.01	0.08	10.54	b.d.*	99.45	0.42	⋯	1.29	0.95	0.98	⋯	0.00	0.00	0.29	0.00	3.94(6)	⋯
Rim pyroxene-1	12.44	0.13	38.47	16.84	23.36	2.16	0.01	0.12	5.07	0.04	98.63	0.70	0.01	1.44	0.74	0.94	0.07	0.00	0.00	0.14	0.00	4.05(6)	⋯

Table 6

(Continued)

	Oxides wt%											Atomic Number per Formula Unit											
	MgO	Na_2O	SiO_2	Al_2O_3	CaO	FeO	K_2O	Cr_2O_3	TiO_2	MnO	Total	Mg	Na	Si	Al	Ca	Fe	K	Cr	Ti	Mn	Total[a]	Åk Content
Rim pyroxene-2	17.17	0.23	53.05	3.52	23.55	2.07	0.02	0.06	0.28	0.01	99.96	0.93	0.02	1.92	0.15	0.91	0.06	0.00	0.00	0.01	0.00	4.00(6)	⋯
Rim pyroxene-3	11.74	0.21	50.82	1.85	22.62	12.79	0.01	0.05	0.11	0.05	100.25	0.67	0.02	1.93	0.08	0.92	0.41	0.00	0.00	0.00	0.00	4.03(6)	⋯
Rim pyroxene-4	17.35	0.02	53.30	3.24	25.39	0.55	0.01	0.06	0.03	0.01	99.96	0.93	0.00	1.93	0.14	0.98	0.02	0.00	0.00	0.00	0.00	4.00(6)	⋯
Rim pyroxene-5	18.24	b.d.*	54.29	1.44	25.86	0.38	b.d.*	0.04	b.d.*	0.01	100.26	0.98	0.00	1.96	0.06	1.00	0.01	0.00	0.00	⋯	0.00	4.01(6)	⋯
Rim pyroxene-6	15.14	0.32	42.46	15.96	19.33	4.58	0.06	0.07	1.75	0.02	99.70	0.83	0.02	1.56	0.69	0.76	0.14	0.00	0.00	0.05	0.00	4.06(6)	⋯
Interior melilite-1	3.03	b.d.*	25.99	29.55	40.77	0.10	b.d.*	b.d.*	b.d.*	0.02	99.46	0.21	0.00	1.19	1.60	2.00	0.00	⋯	⋯	⋯	0.00	5.01(7)	21
Interior melilite-2	3.21	0.01	26.17	29.00	40.49	0.12	b.d.*	b.d.*	0.02	b.d.*	99.02	0.22	0.00	1.21	1.57	2.00	0.00	⋯	⋯	0.00	⋯	5.01(7)	22
Interior melilite-3	2.98	0.02	25.86	29.43	40.28	0.32	b.d.*	0.01	0.03	0.01	98.93	0.20	0.00	1.19	1.60	1.99	0.01	⋯	0.00	0.00	0.00	5.01(7)	20
Interior melilite-4	2.23	0.01	24.87	31.89	40.57	0.28	b.d.*	b.d.*	0.01	b.d.*	99.87	0.15	0.00	1.14	1.72	1.99	0.01	⋯	⋯	0.00	⋯	5.00(7)	15
Interior melilite-5	3.70	0.02	27.32	27.90	40.68	0.18	0.01	0.02	0.03	b.d.*	99.87	0.25	0.00	1.25	1.50	1.99	0.01	0.00	0.00	0.00	⋯	5.00(7)	25
Interior melilite-6	6.32	0.02	31.36	20.63	40.53	b.d*	0.01	0.02	0.06	0.01	98.95	0.43	0.00	1.44	1.12	2.00	0.00	0.00	0.00	0.00	0.00	5.00(7)	43
Interior melilite-7	4.14	0.01	27.78	26.50	40.64	b.d.*	b.d.*	b.d.*	b.d.*	b.d.*	99.08	0.28	0.00	1.28	1.44	2.00	0.00	⋯	⋯	⋯	⋯	5.00(7)	28
Interior melilite-8	4.60	b.d.*	28.62	25.09	40.68	b.d.*	b.d.*	0.02	b.d.*	b.d.*	99.01	0.32	0.00	1.32	1.36	2.01	0.00	⋯	0.00	⋯	⋯	5.00(7)	32
Interior melilite-9	4.56	0.02	28.43	24.90	40.64	0.03	b.d.*	b.d.*	b.d.*	b.d.*	98.58	0.31	0.00	1.32	1.36	2.01	0.00	⋯	⋯	⋯	⋯	5.01(7)	31
Interior melilite-10	4.72	0.04	28.66	24.80	40.80	0.01	b.d.*	b.d.*	b.d.*	b.d.*	99.03	0.32	0.00	1.32	1.35	2.01	0.00	⋯	⋯	⋯	⋯	5.01(7)	32
Interior melilite-11	4.41	0.02	27.92	26.15	40.71	0.03	b.d.*	0.01	b.d.*	b.d.*	99.25	0.30	0.00	1.28	1.42	2.00	0.00	⋯	0.00	⋯	⋯	5.01(7)	30

Note.

[a] Number of O atoms in the structural formulae.

Table 7
Elemental Composition of Mineral Phases in Organ Pipe

	Oxides wt%											Atomic Number per Formula Unit											
	MgO	Na$_2$O	SiO$_2$	Al$_2$O$_3$	CaO	FeO	K$_2$O	Cr$_2$O$_3$	TiO$_2$	MnO	Total	Mg	Na	Si	Al	Ca	Fe	K	Cr	Ti	Mn	Total[a]	Åk Content
Interior anorthite-1	0.10	0.03	41.66	37.30	20.19	0.01	b.d.*	b.d.*	0.02	0.02	99.34	0.01	0.00	1.95	2.06	1.01	0.00	⋯	⋯	0.00	0.00	5.03(8)	⋯
Interior anorthite-2	0.01	0.01	41.78	36.99	20.22	0.04	0.01	0.01	0.02	0.02	99.10	0.00	0.00	1.96	2.04	1.01	0.00	0.00	0.00	0.00	0.00	5.02(8)	⋯
Interior anorthite-3	0.03	0.04	42.00	37.43	20.30	0.06	0.01	b.d.*	0.03	0.02	99.93	0.00	0.00	1.95	2.05	1.01	0.00	0.00	⋯	0.00	0.00	5.02(8)	⋯
Interior anorthite-4	0.04	0.04	42.07	37.01	20.27	0.03	0.01	b.d.*	0.04	b.d.*	99.51	0.00	0.00	1.96	2.04	1.01	0.00	0.00	⋯	0.00	⋯	5.02(8)	⋯
Interior anorthite-5	0.02	0.04	41.82	37.06	20.28	0.05	0.01	b.d.*	0.05	0.01	99.32	0.00	0.00	1.96	2.04	1.02	0.00	0.00	⋯	0.00	0.00	5.02(8)	⋯
Interior anorthite-6	0.03	0.05	42.16	36.83	20.25	0.04	0.01	0.01	0.04	b.d.*	99.43	0.00	0.00	1.97	2.03	1.01	0.00	0.00	0.00	0.00	⋯	5.02(8)	⋯
Interior anorthite-7	0.01	0.03	42.28	37.08	20.30	0.01	b.d.*	0.01	0.03	b.d.*	99.76	0.00	0.00	1.97	2.03	1.01	0.00	⋯	0.00	0.00	⋯	5.02(8)	⋯
Interior anorthite-8	0.04	0.04	41.97	37.00	20.26	0.01	0.01	0.02	0.08	b.d.*	99.43	0.00	0.00	1.96	2.04	1.01	0.00	0.00	0.00	0.00	⋯	5.02(8)	⋯
Interior anorthite-9	0.05	0.05	42.19	36.71	20.28	0.03	0.01	0.01	0.05	b.d.*	99.38	0.00	0.00	1.97	2.02	1.02	0.00	0.00	0.00	0.00	⋯	5.02(8)	⋯
Interior anorthite-10	0.11	0.03	41.86	36.89	20.25	0.01	0.01	b.d.*	0.01	b.d.*	99.17	0.01	0.00	1.96	2.04	1.02	0.00	0.00	⋯	0.00	⋯	5.02(8)	⋯
Interior anorthite-11	0.06	0.03	42.56	36.67	20.26	b.d.*	b.d.*	0.01	0.01	b.d.*	99.59	0.00	0.00	1.98	2.01	1.01	⋯	⋯	0.00	0.00	⋯	5.01(8)	⋯
Interior anorthite-12	0.09	0.08	42.26	37.11	20.16	0.24	0.01	0.01	0.01	0.03	100.02	0.01	0.01	1.96	2.03	1.00	0.01	0.00	0.00	0.00	0.00	5.02(8)	⋯
Interior anorthite-13	0.11	0.03	41.93	36.84	20.22	0.01	b.d.*	0.01	0.01	0.01	99.17	0.01	0.00	1.96	2.03	1.01	0.00	⋯	0.00	0.00	0.00	5.02(8)	⋯
Interior anorthite-14	0.02	0.02	42.26	36.93	20.14	b.d.*	0.01	0.01	0.02	b.d.*	99.42	0.00	0.00	1.97	2.03	1.01	⋯	0.00	0.00	0.00	⋯	5.01(8)	⋯
Interior anorthite-15	0.11	0.04	42.09	36.64	20.16	b.d.*	0.01	0.01	0.04	b.d.*	99.09	0.01	0.00	1.97	2.02	1.01	b.d.	0.00	0.00	0.00	b.d.	5.02(8)	⋯
Rim anorthite-1	1.43	0.09	39.94	39.28	18.98	0.71	0.01	b.d.*	0.02	b.d.*	100.45	0.10	0.01	1.85	2.15	0.94	0.03	0.00	⋯	0.00	⋯	5.08(8)	⋯
Rim anorthite-2	0.23	0.12	41.77	37.52	20.10	0.26	0.01	0.01	b.d.*	0.01	100.03	0.02	0.01	1.94	2.06	1.00	0.01	0.00	0.00	⋯	0.00	5.04(8)	⋯
Rim anorthite-3	0.12	0.05	41.80	37.64	20.26	0.26	0.01	0.01	0.01	0.01	100.16	0.01	0.00	1.94	2.06	1.01	0.01	0.00	0.00	0.00	0.00	5.03(8)	⋯
Rim anorthite-4	0.11	0.03	42.58	36.03	20.20	0.35	b.d.*	b.d.*	0.01	0.03	99.33	0.01	0.00	1.99	1.99	1.01	0.01	⋯	⋯	0.00	0.00	5.02(8)	⋯
Rim anorthite-5	0.79	0.10	40.10	37.76	19.70	0.38	0.01	b.d.*	0.02	b.d.*	98.85	0.06	0.01	1.89	2.10	1.00	0.01	0.00	⋯	0.00	⋯	5.06(8)	⋯
Rim anorthite-6	0.12	0.06	42.10	37.33	20.27	0.15	b.d.*	b.d.*	b.d.*	0.01	100.05	0.01	0.01	1.95	2.04	1.01	0.01	⋯	⋯	⋯	0.00	5.03(8)	⋯
Rim anorthite-7	0.06	0.10	40.87	36.41	20.39	0.14	0.01	b.d.*	0.01	b.d.*	97.99	0.00	0.01	1.94	2.04	1.04	0.01	0.00	b.d.	0.00	b.d.	5.04(8)	⋯
Rim anorthite-8	0.03	0.06	42.06	37.04	20.26	0.06	b.d.*	b.d.*	0.04	b.d.*	99.57	0.00	0.01	1.96	2.04	1.01	0.00	⋯	⋯	0.00	⋯	5.02(8)	⋯
Rim anorthite-9	0.97	0.07	39.87	39.32	19.41	0.59	b.d.*	0.01	0.02	b.d.*	100.27	0.07	0.01	1.85	2.15	0.97	0.02	⋯	0.00	0.00	⋯	5.07(8)	⋯
Rim anorthite-10	0.21	0.10	41.29	36.51	21.07	0.16	0.01	b.d.*	0.02	b.d.*	99.38	0.01	0.01	1.94	2.02	1.06	0.01	0.00	⋯	0.00	⋯	5.05(8)	⋯
Rim anorthite-11	0.02	0.04	41.94	37.16	20.47	0.16	0.01	b.d.*	b.d.*	0.02	99.82	0.00	0.00	1.95	2.04	1.02	0.01	0.00	⋯	⋯	0.00	5.03(8)	⋯
Rim anorthite-12	b.d.*	0.04	41.86	36.84	20.28	0.18	0.02	0.01	0.01	b.d.*	99.24	b.d.	0.00	1.96	2.03	1.02	0.01	0.00	0.00	0.00	⋯	5.02(8)	⋯
Rim anorthite-13	0.05	0.06	41.31	37.40	20.70	0.13	b.d.*	b.d.*	b.d.*	b.d.*	99.66	0.00	0.01	1.93	2.06	1.04	0.01	⋯	⋯	⋯	⋯	5.04(8)	⋯
Rim anorthite-14	1.15	0.12	42.05	37.92	19.34	0.22	b.d.*	b.d.*	0.02	0.02	100.85	0.08	0.01	1.93	2.06	0.95	0.01	⋯	⋯	0.00	0.00	5.04(8)	⋯
Rim anorthite-15	0.03	0.02	41.85	36.99	20.43	0.19	b.d.*	b.d.*	b.d.*	b.d.*	99.51	0.00	0.00	1.96	2.04	1.02	0.01	⋯	⋯	⋯	⋯	5.03(8)	⋯
Rim anorthite-16	0.02	0.04	42.63	36.89	20.26	0.16	b.d.*	0.01	b.d.*	b.d.*	100.02	0.00	0.00	1.98	2.02	1.01	0.01	⋯	0.00	⋯	⋯	5.01(8)	⋯
Rim anorthite-17	0.14	0.04	42.11	36.92	20.30	0.21	b.d.*	0.01	0.01	0.01	99.76	0.01	0.00	1.96	2.03	1.01	0.01	⋯	0.00	0.00	0.00	5.03(8)	⋯
Rim anorthite-18	0.01	0.04	41.93	36.91	20.06	0.23	0.01	b.d.*	b.d.*	0.01	99.20	0.00	0.00	1.96	2.04	1.01	0.01	0.00	⋯	⋯	0.00	5.02(8)	⋯
Interior spinel-1	27.40	b.d.*	0.05	71.59	0.05	b.d*	b.d.*	0.20	0.35	b.d.*	99.64	0.97	⋯	0.00	2.00	0.00	0.00	⋯	0.00	0.01	⋯	2.99(4)	⋯
Interior spinel-2	27.44	b.d.*	0.05	71.62	0.06	0.04	b.d.*	0.19	0.32	b.d.*	99.73	0.97	⋯	0.00	2.00	0.00	0.00	⋯	0.00	0.01	⋯	2.99(4)	⋯
Interior spinel-3	27.94	b.d.*	0.05	72.02	0.09	0.07	0.01	0.18	0.27	b.d.*	100.62	0.98	⋯	0.00	2.00	0.00	0.00	0.00	0.00	0.00	⋯	2.99(4)	⋯
Interior spinel-4	27.77	b.d.*	0.05	71.75	0.09	0.13	b.d.*	0.19	0.31	0.01	100.30	0.98	⋯	0.00	2.00	0.00	0.00	⋯	0.00	0.01	0.00	2.99(4)	⋯
Interior spinel-5	27.88	b.d.*	0.05	71.83	0.10	0.08	b.d.*	0.20	0.30	0.02	100.47	0.98	⋯	0.00	2.00	0.00	0.00	⋯	0.00	0.01	0.00	2.99(4)	⋯
Interior spinel-6	28.08	b.d.*	0.07	71.89	0.10	b.d.*	b.d.*	0.14	0.38	0.01	100.69	0.99	⋯	0.00	1.99	0.00	0.00	⋯	0.00	0.01	0.00	2.99(4)	⋯
Interior spinel-7	27.48	b.d.*	0.03	71.71	0.08	b.d.*	b.d.*	0.21	0.27	b.d.*	99.78	0.97	⋯	0.00	2.01	0.00	0.00	⋯	0.00	0.00	⋯	2.99(4)	⋯
Interior spinel-8	27.61	b.d.*	0.03	71.73	0.08	0.00	0.01	0.18	0.29	b.d.*	99.92	0.98	⋯	0.00	2.00	0.00	0.00	0.00	0.00	0.01	⋯	2.99(4)	⋯
Interior spinel-9	27.70	b.d.*	0.04	72.13	0.11	0.01	0.01	0.20	0.28	b.d.*	100.48	0.97	⋯	0.00	2.00	0.00	0.00	0.00	0.00	0.00	⋯	2.99(4)	⋯
Interior spinel-10	27.53	b.d.*	0.04	71.68	0.08	0.04	b.d.*	0.17	0.32	b.d.*	99.85	0.97	⋯	0.00	2.00	0.00	0.00	⋯	0.00	0.01	⋯	2.99(4)	⋯
Rim spinel-1	26.70	0.01	0.24	70.89	0.22	1.16	b.d.*	0.13	0.32	0.02	99.69	0.95	0.00	0.01	2.00	0.01	0.02	b.d.	0.00	0.01	0.00	2.99(4)	⋯
Rim spinel-2	27.59	b.d.*	0.11	71.77	0.16	0.49	b.d.*	0.11	0.30	b.d.*	100.52	0.97	⋯	0.00	2.00	0.00	0.01	⋯	0.00	0.01	⋯	2.99(4)	⋯
Rim spinel-3	26.44	b.d.*	0.23	70.28	0.62	1.26	b.d.*	0.17	0.75	b.d.*	99.75	0.94	⋯	0.01	1.98	0.02	0.03	⋯	0.00	0.01	⋯	2.99(4)	⋯
Rim spinel-4	24.78	b.d.*	0.10	69.98	0.09	4.83	b.d.*	0.14	0.18	0.03	100.12	0.89	⋯	0.00	1.99	0.00	0.10	⋯	0.00	0.00	0.00	3.00(4)	⋯

Table 7
(Continued)

	Oxides wt%											Atomic Number per Formula Unit											
	MgO	Na_2O	SiO_2	Al_2O_3	CaO	FeO	K_2O	Cr_2O_3	TiO_2	MnO	Total	Mg	Na	Si	Al	Ca	Fe	K	Cr	Ti	Mn	Total[a]	Åk Content
Rim spinel-5	24.21	0.01	0.10	69.63	0.09	5.86	b.d.*	0.14	0.24	0.02	100.31	0.88	0.00	0.00	1.99	0.00	0.12	⋯	0.00	0.00	0.00	3.00(4)	⋯
Interior pyroxene-1	9.51	b.d.*	38.60	19.37	25.34	b.d.*	b.d.*	0.04	6.22	b.d.*	99.10	0.52	⋯	1.43	0.84	1.00	⋯	⋯	0.00	0.17	⋯	3.98(6)	⋯
Interior pyroxene-2	8.55	b.d.*	37.47	21.01	25.01	0.01	b.d.*	0.04	7.44	b.d.*	99.55	0.47	⋯	1.38	0.91	0.99	0.00	⋯	0.00	0.21	⋯	3.96(6)	⋯
Interior pyroxene-3	8.85	0.01	37.73	20.53	25.04	b.d.*	b.d.*	0.03	7.16	0.02	99.38	0.49	0.00	1.39	0.89	0.99	⋯	⋯	0.00	0.20.	0.00	3.96(6)	⋯
Interior pyroxene-4	9.31	b.d.*	38.36	18.60	25.01	0.04	0.01	0.05	8.02	0.01	99.42	0.51	b.d.	1.42	0.81	0.99	0.00	0.00	0.00	0.22	0.00	3.96(6)	⋯
Interior pyroxene-5	8.79	b.d.*	37.00	19.39	25.10	0.01	b.d.*	0.06	8.87	b.d.*	99.22	0.49	⋯	1.37	0.85	1.00	0.00	⋯	0.00	0.25	⋯	3.95(6)	⋯
Interior pyroxene-6	8.79	b.d.*	36.68	19.36	24.85	0.03	b.d.*	0.04	9.32	b.d.*	99.07	0.49	⋯	1.36	0.85	0.99	0.00	⋯	0.00	0.26	⋯	3.95(6)	⋯
Interior pyroxene-7	7.47	0.01	34.01	22.20	24.64	0.01	b.d.*	0.04	10.59	b.d.*	98.98	0.42	0.00	1.27	0.98	0.99	0.00	⋯	0.00	0.30	⋯	3.95(6)	⋯
Interior pyroxene-8	8.91	0.01	37.43	18.38	24.87	b.d.*	0.01	0.04	9.42	0.02	99.09	0.49	0.00	1.39	0.80	0.99	⋯	0.00	0.00	0.26	0.00	3.94(6)	⋯
Interior pyroxene-9	9.19	b.d.*	37.87	20.39	25.14	0.04	b.d.*	0.04	6.55	0.01	99.22	0.51	⋯	1.40	0.89	1.00	0.00	⋯	0.00	0.18	0.00	3.97(6)	⋯
Interior pyroxene-10	11.17	0.01	41.37	15.87	25.25	0.01	b.d.*	0.05	5.54	b.d.*	99.27	0.61	0.00	1.52	0.69	1.00	0.00	⋯	0.00	0.15	⋯	3.98(6)	⋯
Interior pyroxene-11	9.29	b.d.*	38.34	19.83	25.17	b.d.*	b.d.*	0.04	6.69	b.d.*	99.36	0.51	⋯	1.41	0.86	0.99	⋯	⋯	0.00	0.19	⋯	3.97(6)	⋯
Interior pyroxene-12	9.05	0.01	38.17	20.25	25.16	0.03	b.d.*	0.06	6.74	b.d.*	99.48	0.50	0.00	1.41	0.88	0.99	0.00	b.d.	0.00	0.19	b.d.	3.97(6)	⋯
Rim pyroxene-1	14.81	0.24	49.72	4.47	24.56	4.58	0.01	0.06	0.37	b.d.*	98.83	0.83	0.02	1.86	0.20	0.98	0.14	0.00	0.00	0.01	b.d.	4.04(6)	⋯
Rim pyroxene-2	24.04	0.10	44.60	5.85	14.38	10.59	0.01	0.06	1.78	0.25	101.65	1.32	0.01	1.64	0.25	0.57	0.33	0.00	0.00	0.05	0.01	4.18(6)	⋯
Rim pyroxene-3	14.74	0.32	49.41	3.91	23.34	7.57	0.02	0.08	0.51	0.07	99.97	0.82	0.02	1.85	0.17	0.94	0.24	0.00	0.00	0.01	0.00	4.06(6)	⋯
Rim pyroxene-4	16.58	0.13	51.47	6.18	24.88	0.66	0.02	0.04	0.16	b.d.*	100.12	0.89	0.01	1.86	0.26	0.96	0.02	0.00	0.00	0.00	⋯	4.01(6)	⋯
Rim pyroxene-5	14.04	0.17	46.33	10.74	24.31	2.02	0.03	0.09	1.72	0.03	99.47	0.77	0.01	1.70	0.47	0.96	0.06	0.00	0.00	0.05	0.00	4.02(6)	⋯
Rim pyroxene-6	13.52	0.22	45.39	12.43	22.11	4.54	0.05	0.14	0.81	0.04	99.25	0.75	0.02	1.68	0.54	0.88	0.14	0.00	0.00	0.02	0.00	4.03(6)	⋯
Rim pyroxene-7	12.92	0.17	44.53	11.16	23.80	2.13	0.03	0.12	4.25	0.03	99.13	0.71	0.01	1.65	0.49	0.94	0.07	0.00	0.00	0.12	0.00	3.99(6)	⋯
Interior melilite-1	4.61	b.d.*	28.16	25.06	40.81	b.d.*	b.d.*	b.d.*	0.02	b.d.*	98.66	0.32	⋯	1.30	1.37	2.02	⋯	⋯	⋯	0.00	⋯	5.01(7)	32
Interior melilite-2	3.24	b.d.*	26.03	28.52	40.78	0.01	b.d.*	b.d.*	0.02	b.d.*	98.60	0.22	⋯	1.21	1.56	2.02	0.00	⋯	⋯	0.00	⋯	5.01(7)	22
Interior melilite-3	2.31	0.02	24.57	30.76	40.77	0.02	b.d.*	b.d.*	0.03	b.d.*	98.48	0.16	0.00	1.14	1.68	2.03	0.00	⋯	⋯	0.00	⋯	5.02(7)	16
Interior melilite-4	2.45	b.d.*	24.85	30.60	40.76	0.10	b.d.*	b.d.*	b.d.*	b.d.*	98.77	0.17	⋯	1.15	1.67	2.02	0.00	⋯	⋯	⋯	⋯	5.01(7)	17
Interior melilite-5	3.20	0.01	26.11	28.37	40.97	b.d.*	b.d.*	0.01	b.d.*	0.02	98.68	0.22	0.00	1.21	1.55	2.03	b.d.	b.d.	0.00	b.d.	0.00	5.02(7)	23
Interior melilite-6	3.81	0.01	26.97	27.12	40.92	b.d.*	b.d.*	0.01	0.01	b.d.*	98.86	0.26	0.00	1.25	1.48	2.03	⋯	⋯	0.00	0.00	⋯	5.01(7)	26
Interior melilite-7	4.40	0.01	27.72	25.65	40.71	0.02	b.d.*	b.d.*	b.d.*	b.d.*	98.52	0.30	0.00	1.28	1.40	2.02	0.00	⋯	⋯	⋯	⋯	5.01(7)	30
Interior melilite-8	2.25	b.d.*	24.79	30.50	40.94	0.06	b.d.*	b.d.*	0.02	b.d.*	98.57	0.16	⋯	1.15	1.67	2.04	0.00	⋯	⋯	0.00	⋯	5.01(7)	17
Interior melilite-9	1.88	b.d.*	24.04	31.99	40.89	0.14	0.01	b.d.*	0.01	b.d.*	98.95	0.13	⋯	1.11	1.74	2.03	0.01	0.00	⋯	0.00	⋯	5.02(7)	13
Interior melilite-10	1.81	b.d.*	23.77	31.89	40.64	0.18	b.d.*	0.01	0.01	0.01	98.31	0.13	⋯	1.11	1.75	2.03	0.01	⋯	0.00	0.00	0.00	5.02(7)	12
Interior melilite-11	3.22	0.01	26.19	28.27	40.81	0.08	b.d.*	0.01	0.04	b.d.*	98.64	0.22	0.00	1.21	1.54	2.03	0.00	⋯	0.00	0.00	⋯	5.01(7)	23
Interior melilite-12	1.44	b.d.*	23.61	33.28	40.77	0.07	b.d.*	0.01	0.01	b.d.*	99.19	0.10	⋯	1.09	1.81	2.01	0.00	⋯	0.00	0.00	⋯	5.01(7)	10
Interior melilite-13	4.68	b.d.*	28.41	25.19	41.05	0.02	b.d.*	b.d.*	0.03	b.d.*	99.38	0.32	⋯	1.31	1.36	2.02	0.00	⋯	⋯	0.00	⋯	5.01(7)	32
Interior melilite-14	3.54	0.01	26.79	27.77	40.91	0.01	b.d.*	b.d.*	0.02	0.01	99.06	0.24	0.00	1.24	1.51	2.02	0.00	⋯	⋯	0.00	0.00	5.01(7)	25
Interior melilite-15	2.59	0.01	24.95	30.49	40.76	0.06	b.d.*	b.d.*	0.03	b.d.*	98.90	0.18	0.00	1.15	1.66	2.02	0.00	⋯	⋯	0.00	⋯	5.02(7)	17
Interior melilite-16	3.41	b.d.*	26.90	27.53	41.13	0.03	0.01	0.01	0.02	b.d.*	99.03	0.23	⋯	1.24	1.50	2.03	0.00	0.00	0.00	0.00	⋯	5.01(7)	25
Interior melilite-17	2.11	0.02	24.73	30.96	41.08	0.04	b.d.*	0.01	0.01	b.d.*	98.97	0.15	0.00	1.14	1.69	2.03	0.00	⋯	0.00	0.00	⋯	5.01(7)	16
Interior melilite-18	4.13	0.04	27.20	26.61	40.91	b.d.*	0.01	0.01	0.02	b.d.*	98.92	0.28	0.00	1.26	1.45	2.03	⋯	0.00	0.00	0.00	⋯	5.02(7)	28

Note.
[a] Number of O atoms in the structural formulae.

Appendix B
Supplementary Figures

Here we show backscatter electron images and X-Ray (MgCaAl composite) maps of the CAIs Ocotillo and Organ Pipe describing their textures. Additionally, we report the $\delta^{26}\mathrm{Mg}*$ external reproducibility of various terrestrial standards using NanoSIMS (Figures 8–16).

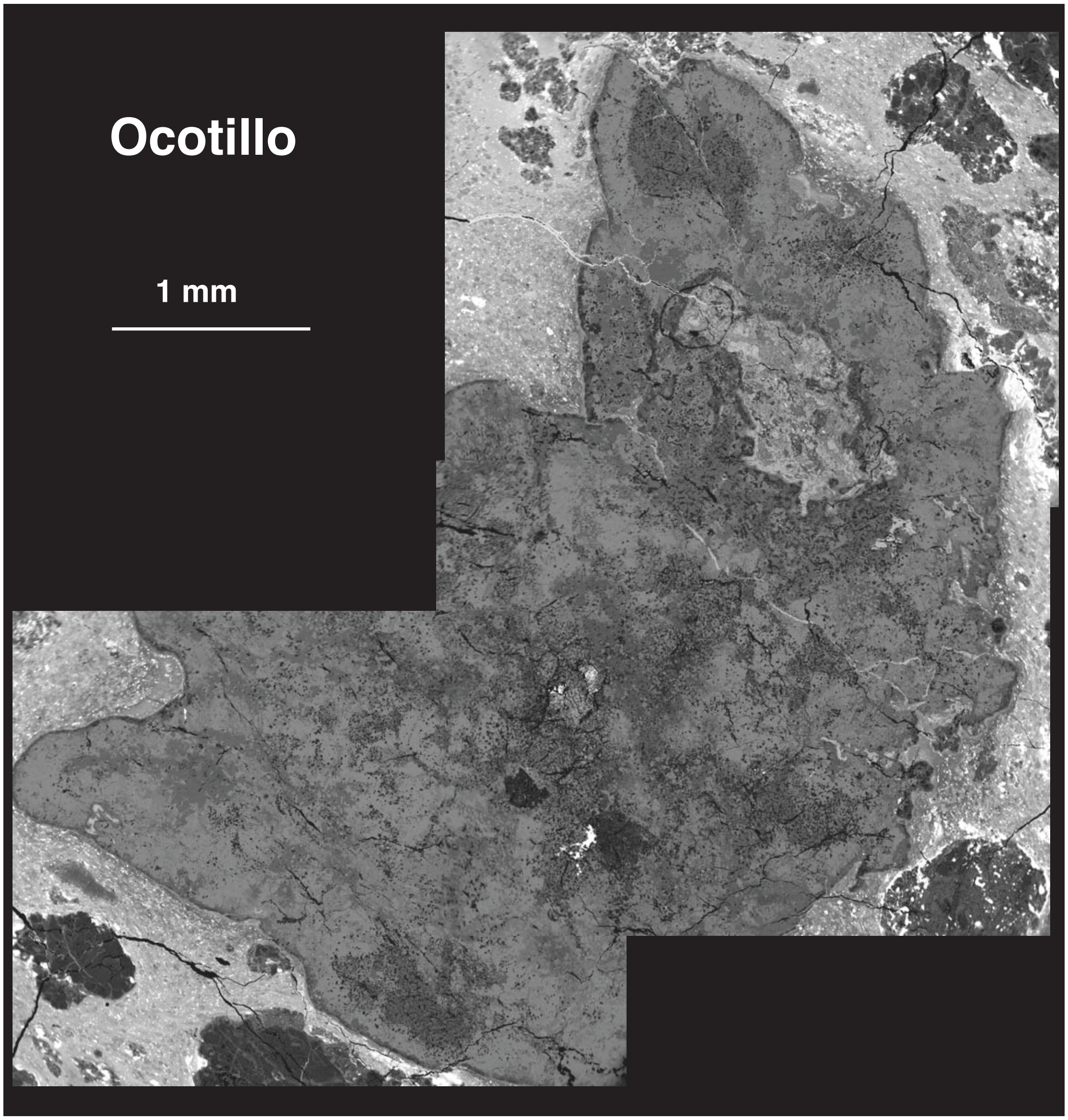

Figure 8. Backscatter electron image of the Ocotillo CAI.

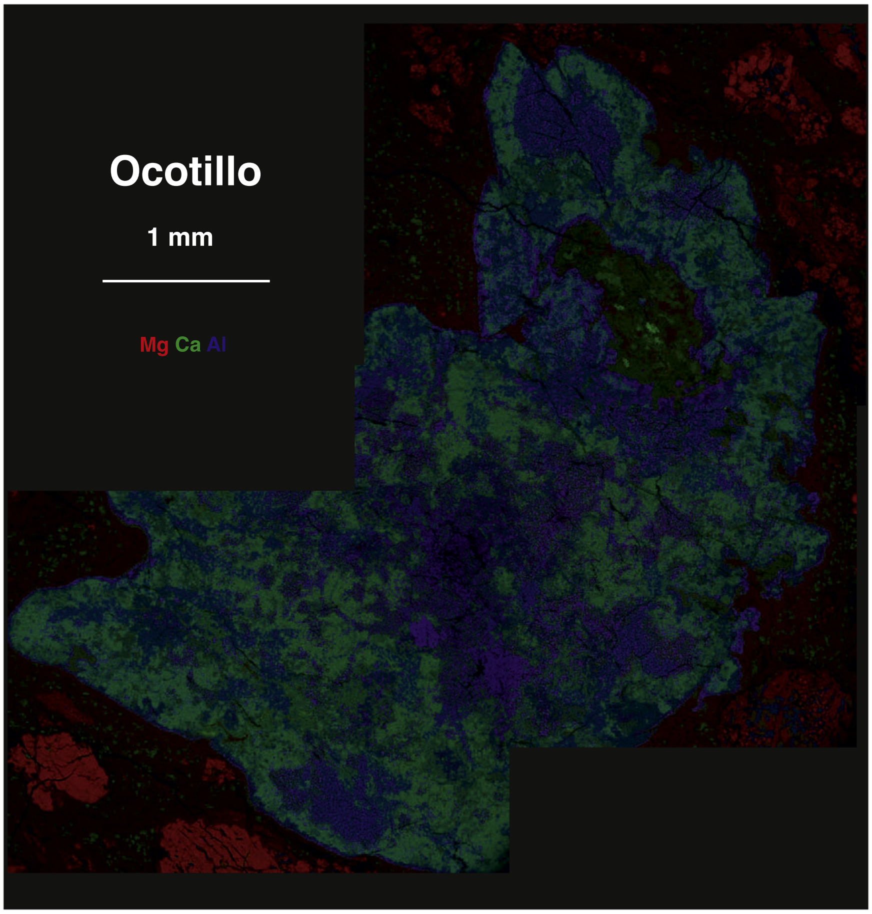

Figure 9. X-ray composition map of the Ocotillo CAI.

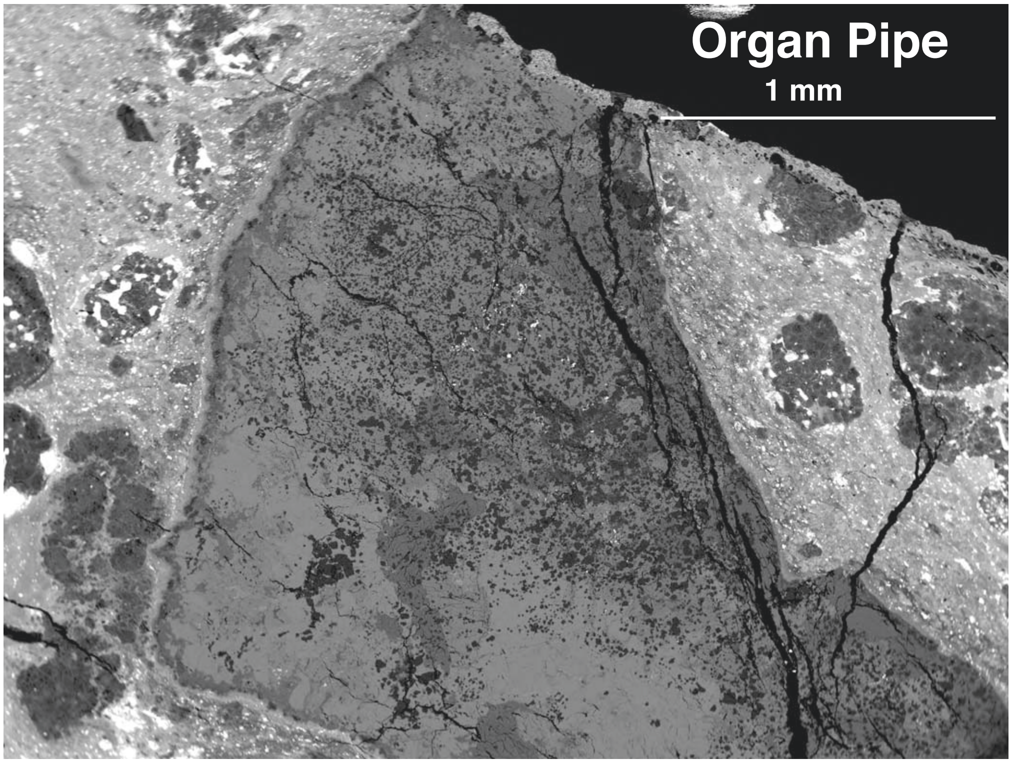

Figure 10. Backscatter electron image of the Organ Pipe CAI.

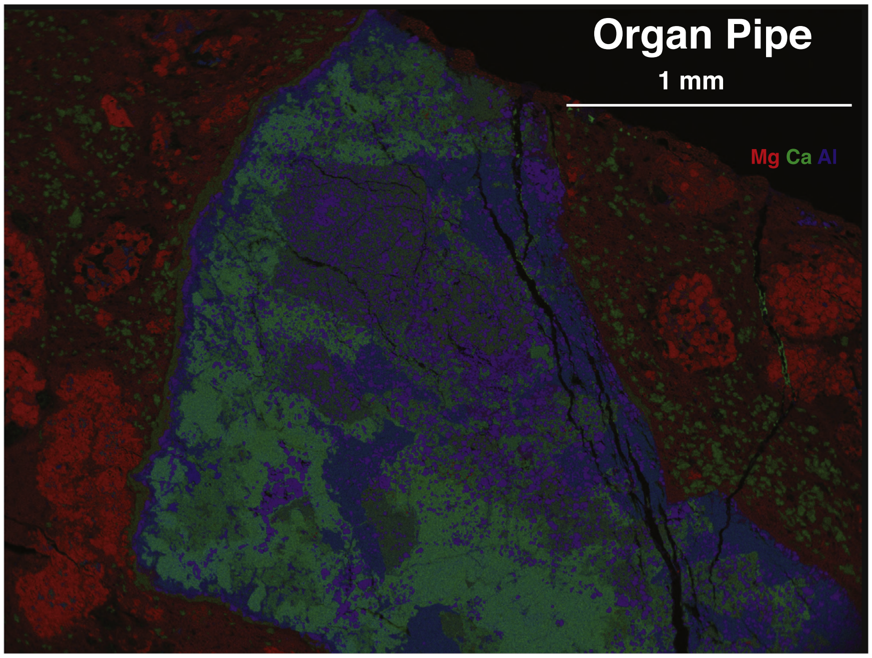

Figure 11. X-ray composition map of the Organ Pipe CAI.

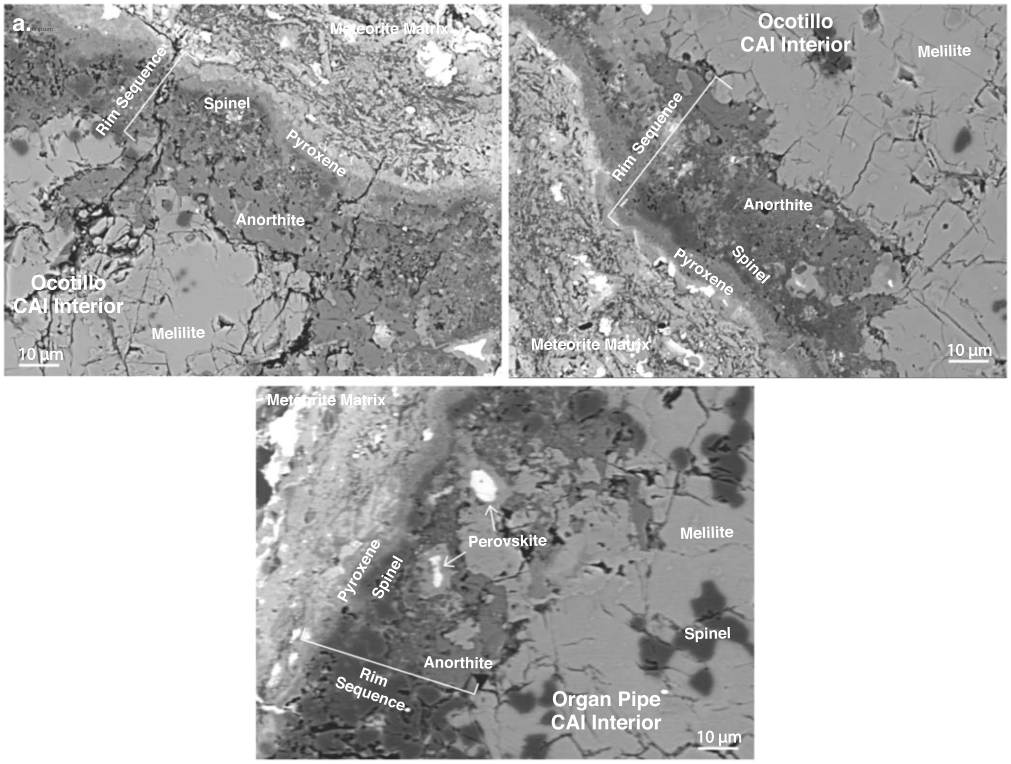

Figure 12. High-resolution backscattered electron images of various regions in the CAIs Ocotillo and Organ Pipe.

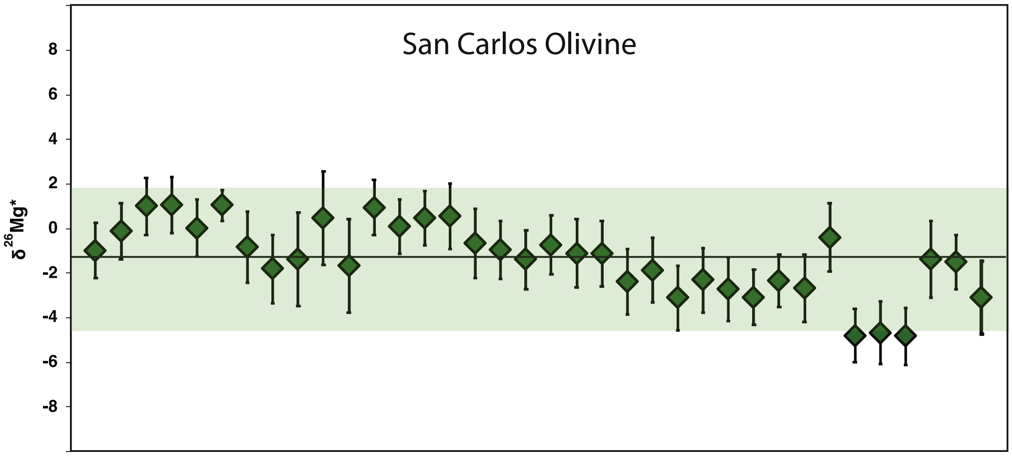

Figure 13. External reproducibility in δ^{26}Mg* for San Carlos olivine standard.

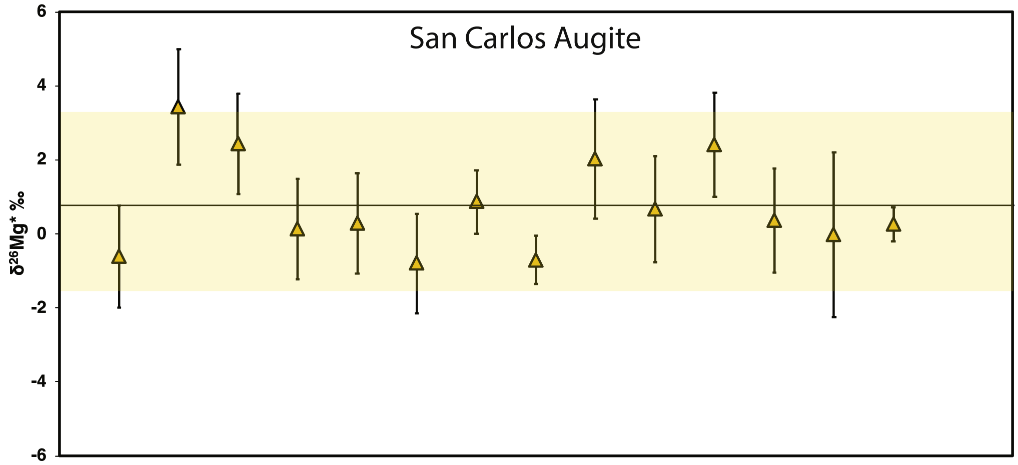

Figure 14. External reproducibility in δ^{26}Mg* for San Carlos augite standard.

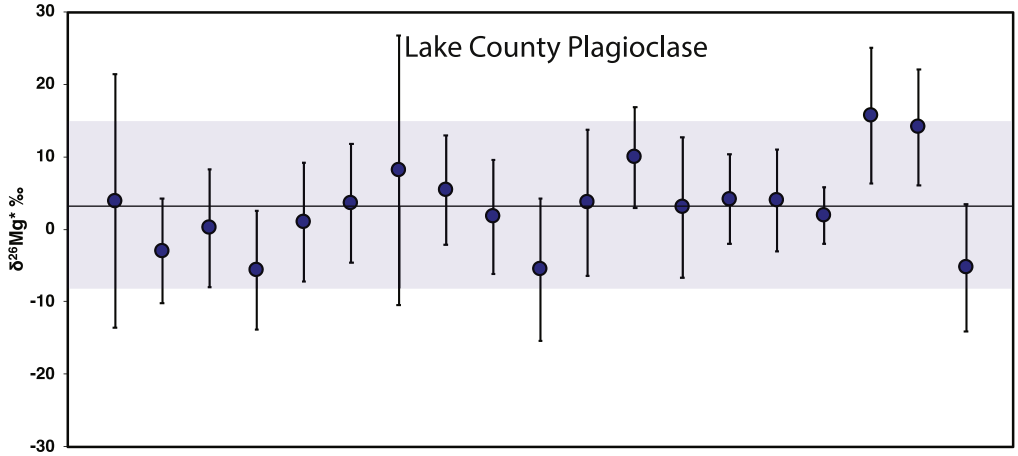

Figure 15. External reproducibility in δ^{26}Mg* for Lake County plagioclase standard.

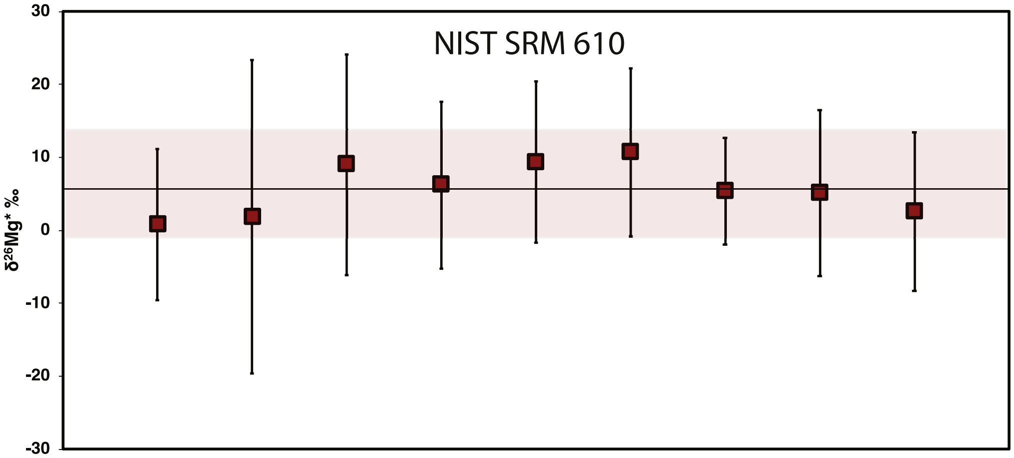

Figure 16. External reproducibility in δ^{26}Mg* for NIST SRM 610 glass standard.

ORCID iDs

Prajkta Mane https://orcid.org/0000-0002-6918-2653
Maitrayee Bose https://orcid.org/0000-0002-7978-6370
Meenakshi Wadhwa https://orcid.org/0000-0001-9187-1255

References

Amelin, Y., Kaltenbach, A., Iizuka, T., et al. 2010, E&PSL, 300, 343
Benisty, M., Juhasz, A., Boccaletti, A., et al. 2015, A&A, 578, L6
Bollard, J., Connelly, J. N., Whitehouse, M. J., et al. 2017, SciA, 3, e1700407
Bollard, J., Kawasaki, N., Sakamoto, N., et al. 2019, GeCoA, 260, 62
Bolser, D., Zega, T. J., Asaduzzaman, A., et al. 2016, M&PS, 51, 743
Bose, M., Root, R., & Pizzarello, S. 2017, M&PS, 52, 546
Boss, A. P. 2008, E&PSL, 268, 102
Boss, A. P., & Durisen, R. 2005, ApJL, 621, L137
Brearley, A., & Jones, R. 1998, Rev. Mineral., 36, 3, https://research.manchester.ac.uk/en/publications/chondritic-meteorites
Budde, G., Kruijer, T. S., & Kleine, T. 2018, GeCoA, 222, 284
Busemann, H., Alexander, M. O., & Nittler, L. R. 2007, M&PS, 42, 1387
Catanzaro, E. J., Murphy, T. J., Garner, E. L., & Shields, W. R. 1966, JRNBS, 70, 453
Ciesla, F. 2010, Icar, 208, 455
Connelly, J. N., Bizzarro, M., Krot, A. N., et al. 2012, Sci, 338, 651
Connolly, H. C., Jr., Desch, S. J., Ash, R. D., & Jones, R. H. 2006, in Meteorites and the Early Solar System II, ed. D. S. Lauretta & H. Y. McSween (Tucson, AZ: Univ. Arizona Press), 383
Cuvillier, P., Leroux, H., Jacob, D., & Hirel, P. 2015, M&PS, 50, 1529
Cuzzi, J. N., Davis, S. S., & Dobrovolskis, A. R. 2003, Icar, 166, 385
Cuzzi, J. N., & Weidenschilling, S. J. 2006, in Meteorites and the Early Solar System II, ed. D. S. Lauretta & H. Y. McSween (Tucson, AZ: Univ. Arizona Press), 353
Dauphas, N., & Pourmand, A. 2011, Natur, 473, 489
Davis, A., & Richter, F. 2014, in Meteorites and Cosmochemical Processes, ed. A. M. Davis (Oxford: Elsevier), 335
Davis, A., Simon, S., & Grossman, L. 1994, in 25th Lunar and Planetary Science Conf., 315
Davis, A. M., MacPherson, G. J., & Hinton, R. W. 1986, Metic, 21, 349
Davis, A. M., Richter, F. M., Mendybaev, R. A., et al. 2015, GeCoA, 158, 245
Desch, S. J., Kalyaan, A., & Alexander, C. M. 2018, ApJS, 238, 11
Desch, S. J., Morris, M. A., Connolly, H. C., Jr., & Boss, A. P. 2012, M&PS, 47, 1139
Doyle, P. M., Jogo, K., Nagashima, K., et al. 2015, NatCo, 6, 7444
Dunham, E. T., Balta, J. B., Wadhwa, M., Sharp, T. G., & McSween, H. Y., Jr. 2019, M&PS, 54, 811
Fagan, T., Guan, Y., & MacPherson, G. 2007, M&PS, 42, 1221
Grossman, L. 1972, GeCoA, 36, 597
Grossman, L., Beckett, J. R., Fedkin, A. V., Simon, S. B., & Ciesla, F. J. 2008, RvMG, 68, 93
Han, J., Keller, L. P., Liu, M.-C., et al. 2020, GeCoA, 269, 639
Heck, P. R., Ushikubo, T., Schmitz, B., et al. 2010, GeCoA, 74, 497
Hinton, R. 1990, ChGeo, 83, 11
Hood, L. L., Ciesla, F. J., Artemieva, N. A., Marzari, F., & Weidenschilling, S. J. 2009, M&PS, 44, 327
Hoppe, P., Cohen, S., & Meibom, A. 2013, Geostand. Geoanal. Res., 37, 111
Hsu, W., Wasserburg, G., & Huss, G. R. 2000, E&PSL, 182, 15
Ito, M., & Messenger, S. 2010, M&PS, 45, 583
Jacobsen, B., Yin, Q.-z., Moynier, F., et al. 2008, E&PSL, 272, 353
Jarosewich, E., Nelen, J., & Norberg, J. A. 1980, Geostand. Newsl., 4, 43
Kawasaki, N., Itoh, S., Sakamoto, N., & Yurimoto, H. 2017, GeCoA, 201, 83
Kita, N. T., Nagahara, H., Tachibana, S., et al. 2010, GeCoA, 74, 6610
Kita, N. T., Yin, Q.-Z., MacPherson, G. J., et al. 2013, M&PS, 48, 1383
Kleine, T., Mezger, K., Palme, H., Scherer, E., & Münker, C. 2005, GeCoA, 69, 5805
Kleine, T., & Wadhwa, M. 2017, in Planetesimals: Early Differentiation and Consequences for Planets, ed. L. T. Elkins-Tanton & B. P. Weiss (Cambridge: Cambridge Univ. Press), 224
Krot, A. N., McKeegan, K. D., Leshin, L. A., MacPherson, G. J., & Scott, E. R. 2002, Sci, 295, 1051
Kruijer, T. S., Burkhardt, C., Budde, G., & Kleine, T. 2017, PNAS, 114, 6712
Kruijer, T. S., Kleine, T., Fischer-Gödde, M., Burkhardt, C., & Wieler, R. 2014, E&PSL, 403, 317
Larsen, K. K., Schiller, M., & Bizzarro, M. 2016, GeCoA, 176, 295
LaTourrette, T., & Wasserburg, G. 1998, E&PSL, 158, 91
MacPherson, G. 2014, Meteorites and Cosmochemical Processes, Vol. 139 (Oxford: Elsevier)
MacPherson, G., Bullock, E., Janney, P., et al. 2010, ApJL, 711, L117
MacPherson, G., Grossman, L., Beckett, J., & Allen, J. 1981, in LUNAR AND PLANETARY SCIENCE XII, 648
MacPherson, G., Kita, N., Ushikubo, T., Bullock, E., & Davis, A. 2012, E&PSL, 331, 43
Macpherson, G. J., & Davis, A. M. 1993, GeCoA, 57, 231
Mane, P., Bose, M., & Wadhwa, M. 2015, in 46th Lunar and Planetary Science Conf., 2898
Mane, P., Wallace, S., Bose, M., et al. 2022, GeCoA, 332, 369
Murrell, M., & Burnett, D. 1986, LPSC, 17, 589
Pignatale, F. C., Jacquet, E., Chaussidon, M., & Charnoz, S. 2019, ApJ, 884, 31
Podosek, F. A., Zinner, E. K., Macpherson, G. J., et al. 1991, GeCoA, 55, 1083
Ruzicka, A., Grossman, J., Bouvier, A., Herd, C. D., & Agee, C. B. 2015, M&PS, 50, 1661
Ryerson, F., & McKeegan, K. D. 1994, GeCoA, 58, 3713
Schiller, M., Connelly, J. N., Glad, A. C., Mikouchi, T., & Bizzarro, M. 2015, E&PSL, 420, 45
Simon, J. I., Hutcheon, I. D., Simon, S. B., et al. 2011, Sci, 331, 1175
Simon, J. I., Matzel, J. E., Simon, S. B., et al. 2016, GeCoA, 186, 242
Simon, J. I., Young, E. D., Russell, S. S., et al. 2005, E&PSL, 238, 272
Thrane, K., Bizzarro, M., & Baker, J. A. 2006, ApJL, 646, L159
Ushikubo, T., Tenner, T. J., Hiyagon, H., & Kita, N. T. 2017, GeCoA, 201, 103
Villeneuve, J., Chaussidon, M., & Libourel, G. 2009, Sci, 325, 985
Wark, D., & Boynton, W. V. 2001, M&PS, 36, 1135
Wark, D., & Lovering, J. 1977, LPSC, 8, 95
Weidenschilling, S. 1977, MNRAS, 180, 57
Weidenschilling, S., Marzari, F., & Hood, L. 1998, Sci, 279, 681
Weinbruch, S., Palme, H., Müller, W., & El Goresy, A. 1990, Metic, 25, 115
Yurimoto, H., Krot, A. N., Choi, B.-G., et al. 2008, RvMG, 68, 141
Zinner, E., & Crozaz, G. 1986, IJMSI, 69, 17